Rate-dependent Electro-mechanical Deformation of Nematic Liquid Crystal Elastomers

Danilo Karličić[a,*], Milan Cajić[a], Stepa Paunović[a], Mokarram Hossain[b]

[a] *Mathematical institute of the Serbian Academy of Sciences and Arts, Kneza Mihaila 36, Belgrade, Serbia*
[b] *Zienkiewicz Centre for Computational Engineering College of Engineering, Bay Campus Swansea University Swansea, United Kingdom*

Abstract

Theoretical modeling and numerical implementation of electro-viscoelastic interactions at finite strains of dielectric nematic Liquid Crystal Elastomers (LCE) are presented, capturing key phenomena such as Maxwell stress, director rotation, nonlinear deformations, the electric Fréedericksz transition, and energy dissipation. By combining continuum mechanics with Maxwell's equations, governing equations for dielectric nematic LCEs are systematically derived via the principle of virtual power. The resulting thermodynamically consistent constitutive relations provide a relevant description of the coupled electro-mechanical and rate-dependent viscoelastic response, thereby enabling a reliable prediction of the material's physical behavior. In addition to the electro-mechanical model, evolution equations for the viscous part of the deformation gradient are formulated using an internal variable approach, capturing the time-dependent dissipation characteristic of a generalized Maxwell's rheological model. These equations are integrated using a fully implicit backward Euler scheme to ensure numerical stability and accuracy. Various deformation modes arising during the Fréedericksz transition are investigated, with particular attention to uniform expansion and thinning in the thickness direction as well as bending actuation observed in bi-layer samples. A fundamentally different actuation mode is demonstrated for bi-layer nematic LCE actuators, where reorganization of internal microstructures under an electric field enables two-sided actuation. Furthermore, electro-mechanical bulk instabilities such as buckling, arising from the combined effects of the Fréedericksz transition and Maxwell stresses, are analyzed. Special attention is given to rate-dependent behavior by demonstrating the effect of the electric potential ramp rate on deformation and on the emergence of buckling instabilities. Compared to classical dielectric elastomers, this behavior represents a more advanced mechanism with significant potential for next-generation active and soft robotic devices. Finally, the numerical simulations capturing the viscoelastic response are validated against experimental results from the literature to assess the accuracy and reliability of the proposed finite deformation model.

Keywords: Nematic elastomers, Finite deformation, Visco-hyperelasticity, Fréedericksz transition, Electro-mechanical buckling.

*Corresponding author
Email address: danilok@mi.sanu.ac.rs (Danilo Karličić)

Contents

1. Introduction

Nematic liquid crystal elastomers (LCEs), form a unique and important class of highly responsive multifunctional materials combining the anisotropy and self-organisation of liquid crystal (LC) molecules [1] with the resilience and flexibility of cross-linked polymeric networks [2–4]. They also display significant programmable and rapid shape changes in reaction to different stimuli like solvents, light, heat, or electric and magnetic fields. The special molecular architecture of LCEs sets them apart from other soft and active materials, making them a top choice for future sensors and actuators in a wide range of applications, including smart structures, biomedical devices, soft robotics [5] and MEMS [6]. Programmability, fast and repeated responses, and shape transition in LCEs can be achieved by patterning the LCs mesogens orientation inside the elastomer matrix into desired multidomain configurations [7].

Recently, it has been demonstrated that LCEs can be utilised to create dielectric elastomers (DEs) with exceptional characteristics, such as spontaneous shape changes, rate dependency, viscous hysteresis and anisotropic permittivity [8], which leads to enhanced electro-mechanical behavior compared to classical DEs [9–11]. This is enabled by the electric field acting on both the polymer network and the LC mesogens, which are tightly coupled through the elastomer matrix. Their interaction leads to the rotation of LCs mesogens that tend to align parallel or perpendicular to the electric field, depending on whether the electric permittivity is greater along or across the nematic order, respectively. This phenomenon in the LC/LCE literature is known as the electric Fréedericksz transition [6, 12–14]. However, since LCs mesogens are connected to the polymeric network, electro-mechanical deformation is caused by the coupling between the Maxwell's stress and the rotation of LCs mesogens. For example, a simple model of a monodomain dielectric LCE free standing plate actuator with compliant electrodes on top and bottom sides, subjected to an external electric field, can exhibit multiple modes of deformation, such as elongation, contraction and shear during electric Fréedericksz transition, as given schematically in Fig.1a. Moreover, by designing a model composed of two elastomer layers, where one layer is a dielectric LCE, it becomes possible to induce bending deformations during the electric Fréedericksz transition under relatively low electric field intensities, see Fig.1b. This feature allows LCE-based structures to work as soft actuators, providing a notable advantage compared to conventional DEs, especially when designed as shape programming structures [15–18].

In monodomain LCEs, the mesogens are uniformly aligned along a director field, a unit vector that describes the local orientation of nematic order, where the degree of alignment is quantified by the scalar order parameter. Based on experimental observations, the director field within the LCEs tends to gradually reorient upon exceeding a threshold value from which it continous to align progressively with the direction of the applied external electric field whose intensity increases. Furthermore, by incorporating a modified semi-soft elastic energy formulation, it has been demonstrated that the electric Fréedericksz transition manifests as a supercritical bifurcation [13]. From a physical perspective, this implies that there is no abrupt rotational jump of the director field in its alignment with the direction of the electric field. Instead, a smooth and continuous transition occurs, evolving from a perpendicular orientation to an almost fully aligned state with the electric field [17]. A general continuum model of dielectric nematic LCEs, which incorporates both the viscous effects of the polymer network and the rotational viscosity of the director through a dissipation function, was proposed by Xu and Huo [13]. Their model captures the electric Fréedericksz transition and the rotation of the director field toward alignment with the electric field. Moreover, they modified semi-soft elastic energy in order to capture properly supercritical property of the Fréedericksz transition in LCE sample.

Furthermore, in [19], the authors propose a thermo-electro-elastic model of LCEs that captures inhomogeneous deformations of LCE membranes under external stimuli. However, the model does not account for the dielectric anisotropy characteristic of nematic LCEs, which is essential for enabling advanced actuation modes and enhancing the functional potential of these materials in soft actuator applications. One of the first analytical models of the electrostriction phenomenon in nematic elastomers was presented by Corbett and Warner in [20]. They demonstrated that electro-elongation induced by an external electrostatic field occurs initially due to the reorientation of nematic directors toward the direction of the electric field, followed subsequently by in-plane deformations of the nematic elastomer driven by Maxwell stresses. Within their theoretical framework, they derived an analytical expression for the critical threshold voltage required to initiate director rotation, and analyzed the conditions under which the pull-in instability and discontinuous rotational jumps of the nematic directors occur. Their model provides a fundamental insight into the electro-mechanical coupling mechanisms in anisotropic soft materials and serves as a basis for further theoretical and experimental investigations. Furthermore, the same authors in [21] theoretically demonstrated that two-

dimensional mechanical deformations can occur in nematic elastomers in response to an electric field applied perpendicular to the initial director orientation. Their analytical study reveals that a threshold voltage can induce director rotation and the accompanying mechanical deformations in LCEs. A related phenomenon is the Fréedericksz transition in nematic gels under the influence of an electric field, as discussed in [22], which provides additional insight into electrically induced reorientation and deformation mechanisms in such materials. Although the phenomenon of flexoelectricity in liquid crystals was discovered long ago, its application and modeling in LCEs has only recently been developed. In the study by Rahmati et al. [23], a fundamental multiphysics model of LCEs was proposed, incorporating the coupled effects of photo-flexoelectricity phenomena with size-dependent mechanical responses. Furthermore, it was demonstrated that the contribution of Frank elasticity, explicitly dependent on the gradient of the director field, plays a significant role in the flexoelectric effect and in the overall thermodynamic stability of the presented model.

The continuum model of an ideal monodomain LCE is based on the well-known "neo-classical" strain-energy function, which describes the elastic free energy of a LCE as a combination of the entropic elasticity of polymer chains and the anisotropic orientation of mesogens [24–26]. This phenomenological model is based on the molecular network theory of rubber where the parameters of the neo-Hookean-type strain-energy density can be derived along with the nematic order through statistical averaging at microscopic scale. To accurately capture nonlinear elastic effects at large strains, more sophisticated hyperelastic models can be employed, such as Gent [27], Ogden [28, 29], six-parameter generic hyperelastic model [30] and Benam-Saccomandi stored energy functions [31]. In addition to the neo-classical energy model for LCE, the literature also introduces corresponding elastic energy formulations that account for the semi-soft elasticity characteristic of LCEs [32]. The fundamental assumption underlying the semi-soft elastic behavior is the ability of the director field to rotate toward the direction of maximum stretch, with little change in the mechanical stress [33]. The basic approach to formulating the semi-soft elastic energy was proposed by Verwey and Warner in 1997 [34], where a semi-soft term is added to the original neo-classical elastic energy formulation. This modification accounts for the effects of changes in chain anisotropy, by introducing constant parameters into the energy formulation. The model is also well-suited for analyzing both small and large deformations, modeling stress responses within the framework of the semi-soft elastic effect [35, 36], and capturing the rotation of the director field. However, it should also be noted that certain limitations exist, particularly regarding the initial angle or the specification of the initial director orientation. One way to address this issue is by introducing a semi-soft parameter that depends on the deformation, and it is assumed that this parameter is a function of the deformation [37].

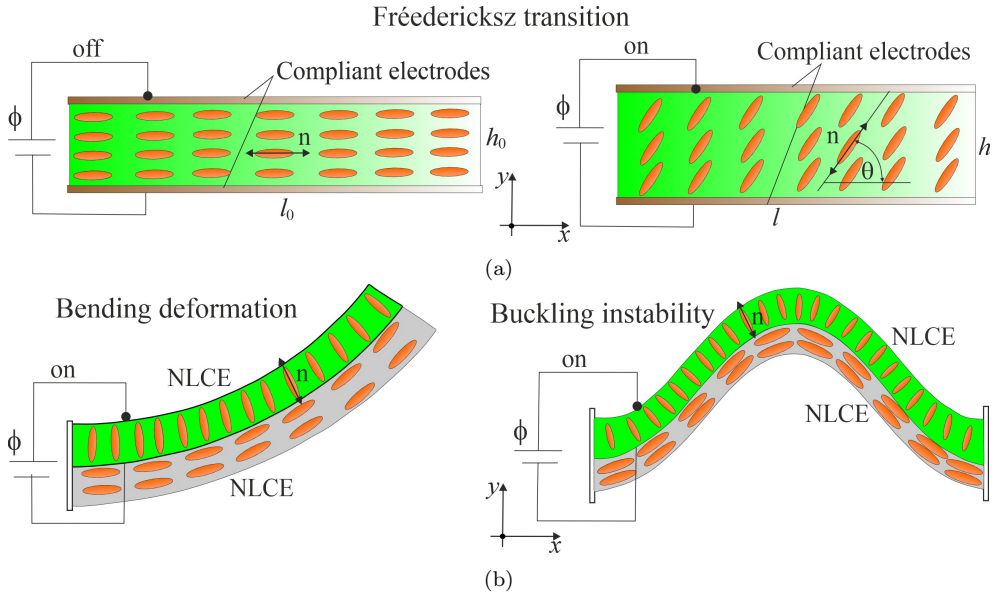

Figure 1: (a) A nematic LCEs sample with an initially distributed director field is subjected to an electrostatic field. The vector **n** represents the director field, which defines the orientation of the nematic microstructure associated with the LC mesogens. Upon applying the electrostatic field, the director field tends to align with the direction of the electric field, resulting in contraction along certain axes [2]. (b) The two-dimensional bi-layer sample consists of a nematic LCE with compliant electrodes, one of which is embedded at the mid-plane of the sample. Application of an external electric field induces bending actuation and buckling instability.

Experimental evidence further suggest that the stress–strain curves of nematic LCEs often exhibit strain-

rate-dependent hysteresis during loading and unloading [38–40]. Formulation of the appropriate viscoelastic models for LCEs must account for dissipation arising from two primary mechanisms: polymer network deformation and viscous rotation of mesogens. The overall material response of LCEs, driven by the interplay between external mechanical loads and environmental stimuli, is typically described by a time-dependent evolution of internal variables that represent both elastic deformations and mesogen reorientation, capturing the inherent viscoelastic nature of the material.

Several modeling strategies have been proposed in the literature to capture the interplay between viscous mesogen rotation and the viscoelastic response of the polymer network [27, 37, 41, 42]. One class of models introduces separate evolution equations for both the viscous deformation and the director field, typically employing an additive decomposition of the total Cauchy stress and couple stress tensors. According to [27, 42], the authors decompose the Cauchy (or the first Piola–Kirchhoff) stress tensor into two components: the first corresponds to the steady-state director rotation, while the second accounts for the viscous contribution from the director dynamics. In general, both the Cauchy stress and couple stress tensors are assumed to consist of steady-state and viscous director rotation components. As highlighted in [43], mesogens are connected to the macromolecules of the polymer network, where elastic and viscoelastic effects dominate over viscous director rotation. This leads to the conclusion that, for comparable strain rates, the evolution equation for the director field can be neglected in the modeling process.

Alternatively, viscoelastic modeling frameworks have been developed to reproduce the experimentally observed rate-dependent behavior by introducing evolution equations for the viscous strain, coupled to the rotation of the director field. In these models, the anisotropy induced by the director orientation is embedded directly into the constitutive formulation of the viscous response, enabling a more accurate representation of the material's directional dependence, both in generalized Maxwell models [37] and Kelvin–Voigt models [44]. This coupling plays a crucial role in capturing the time-dependent mechanical response of nematic LCEs under quasi-static loading. In the present analysis, we adopt this approach for modeling viscoelastic behavior due to its favorable balance between mathematical tractability and physical fidelity, specifically, its ability to capture the key features of anisotropic, time-dependent behavior exhibited by LCEs.

The effects of electric fields on additional dissipation mechanisms, such as dielectric relaxation and current leakage in dielectric LCEs, remain an open question. These phenomena, which are critical for understanding the overall electro-mechanical response of LCEs, have not yet been fully explored. They require careful consideration in future experimental and theoretical studies to improve the predictive accuracy of models and to guide the design of devices under various operating conditions. In the remainder of this study, we adopt a free energy model for nematic LCEs in the form of a modified version of the semi-soft free energy. This formulation is incorporated consistently into both the equilibrium and non-equilibrium branches of the viscoelastic model.

The general framework of continuum thermodynamics, as formulated in the modern approaches of [45] and [46], serves as the foundation for developing a fully nonlinear finite-strain model of dielectric LCEs with a nematic microstructure. The primary motivation of this work is therefore to develop a thermodynamically consistent electro-viscoelastic continuum framework capable of capturing the coupled electric, mechanical, and dissipative mechanisms governing the behavior of dielectric nematic LCEs at finite strains. The model is systematically derived using the principle of virtual power and enriched by internal variables describing viscous deformation, allowing for a generalized Maxwell-type rheological response. Based on this unified theoretical foundation, the numerical examples are specifically designed to elucidate the role of viscoelasticity and director reorganization during electrically driven actuation, including uniform and non-uniform deformation modes, bi-layer bending, two-sided actuation, and electro-mechanical instabilities such as buckling. In this way, both the model development and the numerical simulations are coherently organized around the central goal of understanding and predicting complex, rate-dependent electro-actuation phenomena in nematic LCEs beyond the capabilities of classical DE models.

A review of the literature confirms that the present analysis of nonlinear and viscous electro-mechanical interactions in LCEs is unique in several respects:

- We apply the principle of virtual power to derive the governing equations in the material (Lagrangian) configuration, incorporating an additional balance law for the director field. This is a key feature for accurately modeling the electric Fréedericksz transition under finite-strain regime.

- Second, our approach is based on a nearly incompressible material model for nematic LCEs, characterized by a relatively large bulk modulus. Only the isochoric part of the deformation gradient is used

to formulate the modified semi-soft elastic energy, applied consistently to both equilibrium and non-equilibrium branches of a multi-branch Maxwell-type rheological model combined with Kelvin–Voigt viscous dissipation. While this viscoelastic framework draws inspiration from the model proposed by Zhou et al. [37], it introduces several key modifications tailored to our context.

- Third, we assume that viscous dissipation arises primarily from the polymer network. Consequently, evolution equations are derived only for the viscous part of the deformation gradient. Furthermore, since we incorporate the modified semi-soft model in the non-equilibrium branches of the Maxwell model, along with additional Kelvin–Voigt-type dissipation, the effects of the director field are naturally embedded into the evolution equations. The model is validated by comparing numerical predictions under uniaxial tension with experimental results from the literature, showing fine agreement for viscoelastic response.

- Fourth, to demonstrate the practical applicability of the proposed framework, we simulate the electric actuation of a bi-layer structure composed of a nematic LCE layer with compliant electrodes attached to its top and middle surface. The results show that, under electric stimulation and during the Fréedericksz transition, the director field reorients to align with the electric field direction, producing significant bending deformation of the bi-layer actuator at relatively low voltage. Furthermore, a two-sided actuation mode is observed. At higher electric field intensities, Maxwell stress dominates over the Fréedericksz transition, leading to bending in the opposite direction and the formation of a nearly cylindrical shape of a nematic actuator.

- Finally, we investigate electro-mechanical bulk instability in a nematic LCE's solid-like beam, with a length much greater than its height. The LCE solid-like beam is clamped at left and right edges, mimicking a clamped-clamped beam structure while preserving a full continuum description using the plane-strain formulation. This setup allows for analysis of both mechanical and nematic field variations across the domain. The observed electro-mechanical instability arises from the interplay between the Fréedericksz transition and Maxwell stress which are dominant for higher values of the electric potential, which may induce buckling instabilities. The coupling between these mechanisms can gives rise to create more complex patterns which appear in elastomeric structure, including surface instabilities such as wrinkling and creasing, which will be the subject of future investigations.

The manuscript is organized as follows. Section 2 presents the essential kinematic framework of continuum mechanics, including the fundamental Flory and Sidoroff decomposition of the deformation gradient, which serve as the basis for defining phenomenological finite-strain viscoelasticity. Then, some basic kinematics of nematic microstructures are provided. Section 3 introduces the general formulation of the principle of virtual power, which is employed to derive the balance laws. Sections 4 and 5 address the second law of thermodynamics via the free energy imbalance, followed by the derivation of the associated constitutive and evolution equations. A summary of the governing equations, along with the corresponding boundary and initial conditions, is presented in Section 6. Section 7 outlines the numerical implementation and provides simulation results based on the proposed models. Moreover, the effect of the rate of applied electric voltage on electro-mechanical deformations and buckling will be investigated, in order to highlight the significance of viscoelastic effects and relaxation mechanisms. Finally, concluding remarks and a summary are presented in Section 8.

2. Essential Kinematics

2.1. Kinematics of finite strains

In order to develop the continuum model of dielectric LCEs with nematic microstuctures, we are going to introduce essential kinematic quantities. First of all, we assume the macroscopic body $\mathcal{B}$, with the associated part of the space it occupies in the reference configuration, where $\mathbf{X}$ is an arbitrary position vector of the material point. The general motion of the body $\mathcal{B}$ is represented by the deformation map $\boldsymbol{\chi}(\mathbf{X}, t)$, which is related to the position vector in the current configuration $\mathbf{x} = \boldsymbol{\chi}(\mathbf{X}, t)$. The difference between the position vectors in the referential and the current configurations is introduced through the displacement vector $\mathbf{u} = \boldsymbol{\chi}(\mathbf{X}, t) - \mathbf{X}$. The fundamental kinematic quantities for describing the deformation of the body $\mathcal{B}$, according to [45, 46], are given as:

$$\mathbf{F} = \nabla\boldsymbol{\chi}(\mathbf{X}, t) = \nabla\mathbf{u} + \mathbf{I}, \quad \mathbf{v} = \dot{\boldsymbol{\chi}}(\mathbf{X}, t), \quad \mathbf{a} = \ddot{\boldsymbol{\chi}}(\mathbf{X}, t), \quad \mathbf{L} = \mathrm{grad}\mathbf{v} = \dot{\mathbf{F}}\mathbf{F}^{-1}, \tag{1}$$

where $\mathbf{F}$ is the deformation gradient, $\mathbf{v}$ is the velocity field, $\mathbf{a}$ is the acceleration field, $\mathbf{L}$ is the velocity gradient, $\mathbf{I}$ is a second-order identity tensor and the gradient operator in the material formulation is given as $\nabla\mathbf{u} = \mathrm{Grad}\mathbf{u}$. We assume that the motion is invertible and that the material is impenetrable, which implies that the Jacobian determinant of the deformation gradient satisfies $\mathrm{J} = \det\mathbf{F} > 0$.

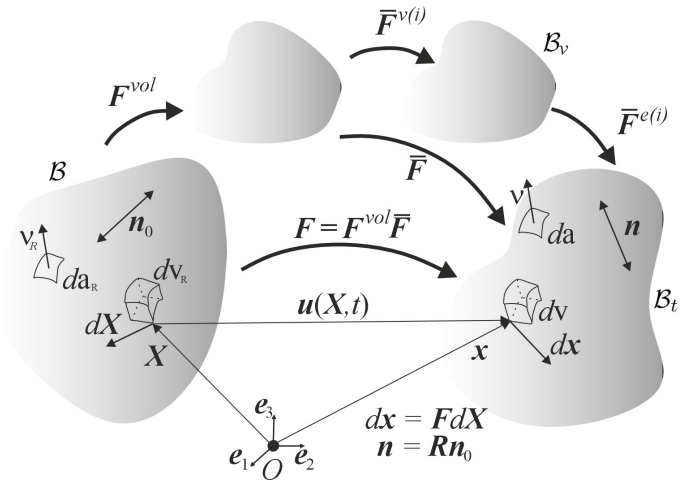

Figure 2: The reference $\mathcal{B}$, intermediate $\mathcal{B}_v$ and current configurations $\mathcal{B}_t$ of the continuum body.

Here we introduced the Flory's decomposition to decouple the volumetric response from the isochoric response (shape deformation). This framework provides a physically consistent, mathematically tractable, and numerically robust approach for constitutive modeling for nearly incompressible materials. Following the Flory's multiplicative decomposition of the deformation gradient $\mathbf{F}$ [46, 47], into the volumetric part $\mathbf{F}^{\mathrm{vol}}$ and the isochoric distortion $\overline{\mathbf{F}}$, yield

$$\mathbf{F} = \mathbf{F}^{vol}\overline{\mathbf{F}} = \mathrm{J}^{1/3}\overline{\mathbf{F}}, \tag{2}$$

where $\det(\overline{\mathbf{F}}) = 1$, representing the incompressibility of the isochoric deformation. Next, we introduce the right and left Cauchy-Green deformation tensors, defined as $\mathbf{C} = \mathbf{F}^T\mathbf{F}$ and $\mathbf{B} = \mathbf{F}\mathbf{F}^T$, respectively. Using the decomposition from (2), these tensors can be expressed as

$$\mathbf{C} = \mathrm{J}^{2/3}\overline{\mathbf{F}}^T\overline{\mathbf{F}} = \mathrm{J}^{2/3}\overline{\mathbf{C}}, \tag{3}$$

$$\mathbf{B} = \mathrm{J}^{2/3}\overline{\mathbf{F}}\,\overline{\mathbf{F}}^T = \mathrm{J}^{2/3}\overline{\mathbf{B}}, \tag{4}$$

where $\overline{\mathbf{C}}$ and $\overline{\mathbf{B}}$ denote the isochoric parts of the right and left Cauchy-Green deformation tensors, respectively.

2.2. Nematic micro-structures

In order to describe the nematic microstructure of the LCE, we introduce a unit vector field in the current configuration $\mathbf{n}$, referred to as the *director field*. This vector field represents the statistical average orientation of the LC molecules - mesogens. To account for the underlying microstructure, we impose an additional constraint that prevents the extensibility of the mesogens [48–50], namely,

$$\mathbf{n}\cdot\mathbf{n} = 1, \tag{5}$$

which ensures that the director remains a unit vector. We define the director field in the reference configuration as

$$\mathbf{n} = \mathbf{R}\mathbf{n}_0, \quad \text{and} \quad \dot{\mathbf{n}} = \boldsymbol{\Omega}^R\mathbf{n}, \tag{6}$$

where $\mathbf{n}_0$ denotes the director in the referential configuration and $\mathbf{R} \in \mathrm{SO}(3)$ is the rotational tensor that can map the reference director to the current director field, with properties $\mathbf{R}^T\mathbf{R} = \mathbf{I}$ and $\det\mathbf{R} = 1$. The present formulation adopts an independent director rotation, consistent with a micropolar continuum framework, in which the director possesses its own balance equation [50, 51]. The tensor $\boldsymbol{\Omega}^R = \dot{\mathbf{R}}\mathbf{R}^T$ is a skew-symmetric tensor associated with rigid-body rotation [46], where the axial vector corresponding to $\boldsymbol{\Omega}^R$ represents the angular velocity of the director.

To describe spatial variations in the orientation of LC molecules in LCEs, we introduce an additional field variable known as the *orientation gradient*, defined as

$$\mathbf{H} = \nabla \mathbf{n}(\mathbf{X}, t). \tag{7}$$

This quantity plays a crucial role in the subsequent analysis, serving both as a thermodynamic state variable and as a penalty term related to the rotation of the director field. It also appears in the definition of the Piola–Frank stress tensor.

2.3. Viscoelastic decomposition

The general framework of the multiplicative decomposition of the deformation gradient was originally developed in plasticity theory [52] and later extended to the analysis of viscoelastic materials. Viscoelastic materials exhibit both an instantaneous elastic response upon loading, and a time-dependent viscous relaxation. By employing the Sidoroff decomposition, these two mechanisms are effectively separated, enabling the instantaneous elastic response and the slower, time-dependent viscous behavior to be modeled independently, yet consistently within the same nonlinear framework. This type of multiplicative decomposition allows the derivation of evolution equations, which are fundamental for tracking the energy dissipation in generalized Maxwell rheological models.

To incorporate the viscoelastic effects in LCEs, we adopt the Sidoroff-type multiplicative decomposition of the deformation gradient within the generalized Maxwell multi-branch model, as proposed in [53–56]:

$$\mathbf{F} = \mathbf{F}^{e(i)}\mathbf{F}^{v(i)}, \quad i = 0, 1, \ldots, N, \tag{8}$$

where $\mathbf{F}^{e(i)}$ and $\mathbf{F}^{v(i)}$ denote the elastic and viscous parts, respectively, of the deformation gradient in the i-th branch. The index $i = 0, 1, \ldots, N$ corresponds to the different viscous relaxation mechanisms represented in the model in Fig.3.

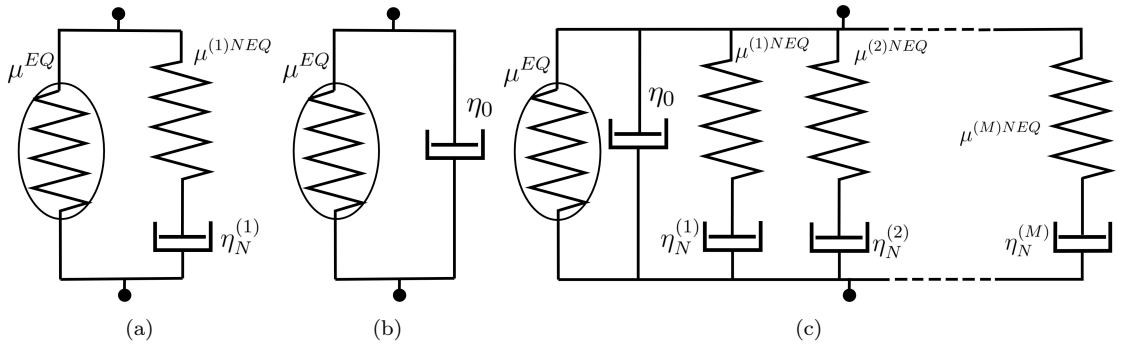

Figure 3: Rheological representations of viscoelastic material models: (a) The Zener model, modified to capture the semi-soft elastic behavior characteristic of nematic LCEs; (b) The Kelvin–Voigt model, representing viscous dissipation; (c) The generalized Maxwell model with additional Kelvin–Voigt-type viscous dissipation, consisting of a single equilibrium branch and M non-equilibrium branches, designed to capture the time-dependent mechanical relaxation and semi-soft elasticity effects of nematic LCEs.

Next, we introduce the Jacobian determinant in its decomposed form as

$$\mathrm{J} = \det \mathbf{F} = \mathrm{J}^{e(i)}\mathrm{J}^{v(i)}, \tag{9}$$

where $\mathrm{J} > 0$ implies that both $\mathrm{J}^{e(i)} > 0$ and $\mathrm{J}^{v(i)} > 0$. Here, $\mathbf{F}^{e(i)}$ and $\mathbf{F}^{v(i)}$ are invertible and correspond to the elastic and viscous parts of the deformation gradient in the i-th branch of the generalized Maxwell model, respectively.

Now, it is possible to decompose the elastic and viscous right and left Cauchy-Green deformation tensors into volumetric and isochoric parts as follows:

$$\mathbf{C}^{e(i)} = \mathrm{J}^{e(i)2/3}\overline{\mathbf{C}}^{e(i)} \quad \text{and} \quad \mathbf{C}^{v(i)} = \mathbf{F}^{v(i)T}\mathbf{F}^{v(i)}, \tag{10}$$

where $\overline{\mathbf{C}}^{e(i)} = \overline{\mathbf{F}}^{e(i)T}\overline{\mathbf{F}}^{e(i)}$ is the isochoric part of the right Cauchy-Green tensor.

Substituting the multiplicative decomposition Eq.(8) into the fourth term of Eq.(1), we obtain the decomposed form of the velocity gradient as

$$\mathbf{L} = \mathbf{L}^{e(i)} + \mathbf{F}^{e(i)}\mathbf{L}^{v(i)}\mathbf{F}^{e(i)-1}, \tag{11}$$

where by a standard definition, the velocity gradient can be decomposed into its symmetric and skew-symmetric parts as

$$\mathbf{L} = \mathbf{D} + \mathbf{W}, \tag{12}$$

and

$$\mathbf{L}^{e(i)} = \dot{\mathbf{F}}^{e(i)}\mathbf{F}^{e(i)-1} = \mathbf{D}^{e(i)} + \mathbf{W}^{e(i)}, \tag{13}$$

$$\mathbf{L}^{v(i)} = \dot{\mathbf{F}}^{v(i)}\mathbf{F}^{v(i)-1} = \mathbf{D}^{v(i)} + \mathbf{W}^{v(i)}, \tag{14}$$

where the tensor fields $\mathbf{D}$ and $\mathbf{W}$ represent the strain rate and spin tensors, respectively.

It should be noted that for numerical implementation of the finite strain viscoelastic model of the LCE, Sidoroff's decomposition allows the elastic and viscous components to be discretized independently, thereby enhancing the stability and convergence of the solution [56].

3. The virtual power principle

3.1. General insights

To derive the governing equations for a continuum model of LCEs, where the nematic microstructure plays a crucial role through the director field, we adopt the principle of virtual power [45, 49, 57, 58]. This generalized principle from continuum mechanics is based on two main requirements:

- For any given portion (or control volume) $\mathcal{P}$ of the body $\mathcal{B}$, the power expended on $\mathcal{P}$, defined for any set of virtual velocities $\mathcal{V}$, is equal to the power expended within $\mathcal{P}$, and is stated as

$$\mathcal{W}_{ext}(\mathcal{P}, \mathcal{V}) = \mathcal{W}_{int}(\mathcal{P}, \mathcal{V}). \tag{15}$$

- For any given portion $\mathcal{P}$ of the body $\mathcal{B}$ and any set of virtual velocities $\mathcal{V}$, the internal power $\mathcal{W}_{\text{int}}(\mathcal{P}, \mathcal{V})$ must satisfy the principle of frame indifference:

$$\mathcal{W}^{+}_{int}(\mathcal{P}, \mathcal{V}^{+}) = \mathcal{W}_{int}(\mathcal{P}, \mathcal{V}). \tag{16}$$

The main reason lies in the fact that it is difficult to prescribe a balance law for the nematic microstructures in advance, since these microstructures involve driving mechanisms that manifest themselves through macroscopic consequences. The derivation of the second requirement of the principle of virtual power can be found in **Appendix A**.

3.2. Balance laws

The first step in applying the principle of virtual power is to define the set of generalized virtual velocities based on the following field variables $(\dot{\boldsymbol{\chi}}, \dot{\mathbf{F}}, \dot{\mathbf{n}}, \dot{\mathbf{H}}, \dot{\phi})$, where we can form the corresponding set of virtual velocities

$$\mathcal{V} = (\tilde{\boldsymbol{\chi}}, \tilde{\mathbf{F}}, \tilde{\mathbf{n}}, \tilde{\mathbf{H}}, \tilde{\phi}), \tag{17}$$

in which variables with tilde ($\tilde{\ }$) define the virtual velocity fields.

Now, we can specify the power expended on $\mathcal{P}$ and the power expended within $\mathcal{P}$ in the reference configuration as

$$\mathcal{W}_{ext}(\mathcal{P}, \mathcal{V}) = \int_{\partial\mathcal{P}} \left(\mathbf{t}_R \cdot \tilde{\boldsymbol{\chi}} + \boldsymbol{\xi}_R \cdot \tilde{\mathbf{n}} + \omega_R \tilde{\phi}\right) da_R + \int_{\mathcal{P}} \left(\mathbf{b}_R \cdot \tilde{\boldsymbol{\chi}} + \boldsymbol{\gamma} \cdot \tilde{\mathbf{n}} + q_R \tilde{\phi}\right) dv_R, \tag{18}$$

and

$$\mathcal{W}_{int}(\mathcal{P}, \mathcal{V}) = \int_{\mathcal{P}} \left(\mathbf{P}_{\text{T}} : \tilde{\mathbf{F}} + \boldsymbol{\Sigma} : \tilde{\mathbf{H}} - \boldsymbol{\pi} \cdot \tilde{\mathbf{n}} + \mathbf{d}_R \cdot \tilde{\mathbf{e}}_R\right) dv_R, \tag{19}$$

where the macroscopic quantities are: $\mathbf{t}_R(\boldsymbol{\nu}_R)$ is the traction vector acting on the boundary with outward unit normal $\boldsymbol{\nu}_R$, $\mathbf{b}_R$ is the external body force per unit reference volume, and $\mathbf{P}_{\text{T}}$ is the total first Piola-Kirchhoff stress tensor. Here, additional scalar terms have to be included in the definition of the virtual power for the electro-mechanical problem. In this formulation, q_R denotes the free charge density, ω_R the free surface charge density, and ϕ the electric potential. For further details on electrostatics, the reader is referred to **Appendix B**. According to [59, 60], the relationship between the total stress tensor and the corresponding Maxwell stress tensor can be derived directly from the principle of virtual work. However, in

this study, we follow the Coleman–Noll procedure to obtain the total stress tensor, where the Maxwell stress tensor represents only one of its components. This approach will be presented in the following section.

The microscopic quantities are: $\boldsymbol{\xi}_R$ is the microscopic traction force with the associated unit vector $\boldsymbol{\nu}_R$, $\boldsymbol{\pi}$ is the internal director body force, $\boldsymbol{\gamma}$ is the external director body force and $\boldsymbol{\Sigma}$ is the orientational stress tensor (the couple stress tensor or microforce stress tensor). According to [49], this approach leads to the derivation of two momentum balance laws, one governing macroscopic deformation and the other governing microscopic (nematic) orientation, together with an angular momentum balance equation arising from the interplay between macroscopic and microscopic torques.

Exploiting the first requirement of the principle of virtual power given in (15), we obtain an explicit formulation for the present case:

$$\int_{\mathcal{P}} \left[(\mathrm{Div}\mathbf{P}_{\mathrm{T}} + \mathbf{b}_R) \cdot \tilde{\boldsymbol{\chi}} + (\mathrm{Div}\boldsymbol{\Sigma} + \boldsymbol{\gamma} + \boldsymbol{\pi}) \cdot \tilde{\mathbf{n}} - (\mathrm{Div}\mathbf{d}_R - q_R)\,\tilde{\phi} \right] dv_R \tag{20}$$

$$= \int_{\partial\mathcal{P}} \left[(\mathbf{P}_{\mathrm{T}}\boldsymbol{\nu}_R - \mathbf{t}_R) \cdot \tilde{\boldsymbol{\chi}} + (\boldsymbol{\Sigma}\boldsymbol{\nu}_R - \boldsymbol{\xi}_R) \cdot \tilde{\mathbf{n}} - (\omega_R + \mathbf{d}_R \cdot \boldsymbol{\nu}_R)\tilde{\phi} \right] da_R,$$

where

$$\mathrm{Div}\mathbf{P}_{\mathrm{T}} + \mathbf{b}_R = \mathbf{0}, \tag{21}$$

$$\mathrm{Div}\boldsymbol{\Sigma} + \boldsymbol{\gamma} + \boldsymbol{\pi} = \mathbf{0}, \tag{22}$$

and

$$\mathrm{Div}\mathbf{d}_R = q_R, \tag{23}$$

which correspond to the balance laws for linear momentum, orientational momentum and Gauss's law, respectively. The Gauss's law derived from the principle of virtual power correspond to the Eq.(B.5) determined in the reference configuration. In the following of the present analysis, the free volume charge density will be neglected ($q_R = 0$), because we assume there are no free charge in the bulk of the LCE sample. The associated traction forces are [46],

$$\mathbf{t}_R = \mathbf{P}_{\mathrm{T}}\boldsymbol{\nu}_R \quad \text{and} \quad \boldsymbol{\xi}_R = \boldsymbol{\Sigma}\boldsymbol{\nu}_R, \tag{24}$$

and the corresponding free-surface charge per unit reference area is

$$\omega_R = -\mathbf{d}_R \cdot \boldsymbol{\nu}_R. \tag{25}$$

In general, the governing equations for nematic LCE can be derived within a micropolar continuum framework, based on the theoretical developments in [51, 61–63] and recent applications in [27, 64]. Moreover, internal body couples $\boldsymbol{\gamma}$ can include torques from electromagnetic sources [61], but their influences are neglected here.

4. The free energy imbalance

4.1. Initial formulation

For the isothermal state, it is possible to reduce the first and second laws of thermodynamics into a single inequality, where the rate of change of free energy and kinetic energy of any arbitrary part $\mathcal{P}$ of the body $\mathcal{B}$ is less than or equal to the total power expended on $\mathcal{P}$. In this case, the Legendre transformation simplifies, and the internal energy density e_R becomes equivalent to the free energy density ψ_R, both defined per unit reference volume. According to Gurtin et al. [45], the free-energy imbalance in integral formulation is given by:

$$\dot{\mathcal{F}} + \dot{\mathcal{K}} \leq \mathcal{W}_{me-ex} + \mathcal{W}_{elec}. \tag{26}$$

We define the following energy and power functionals

1. The total free energy:

$$\mathcal{F}(\mathcal{P}) = \int_{\mathcal{P}} \psi_R dv_R, \tag{27}$$

2. The total kinetic energy:

$$\mathcal{K}(\mathcal{P}) = \int_{\mathcal{P}} \frac{1}{2} \rho_R \mathbf{v} \cdot \mathbf{v} dv_R, \tag{28}$$

where kinetic contributions due to the rotation of the director field are neglected.

The total electro-mechanical power Eq.(18) can be divided on the external mechanical power and electrical power, as it given in the following;

3. The mechanical power expended on $(\mathcal{P})$, by the macroscopic $(\mathbf{t}_R, \mathbf{b}_R)$ and microscopic forces $(\boldsymbol{\xi}_R, \boldsymbol{\gamma})$:

$$\mathcal{W}_{me-ex}(\mathcal{P}) = \int_{\partial\mathcal{P}} (\mathbf{t}_R \cdot \dot{\boldsymbol{\chi}} + \boldsymbol{\xi}_R \cdot \dot{\mathbf{n}}) \, da_R + \int_{\mathcal{P}} (\mathbf{b}_R \cdot \dot{\boldsymbol{\chi}} + \boldsymbol{\gamma} \cdot \dot{\mathbf{n}}) \, dv_R, \tag{29}$$

4. The electric power expended on part $\mathcal{P}$:

$$\mathcal{W}_{elec}(\mathcal{P}) = -\int_{\partial\mathcal{P}} \phi \dot{\mathbf{d}}_R \cdot \boldsymbol{\nu}_R da_R. \tag{30}$$

Using the divergence theorem, and substituting the expressions given in Eq.(24), the balance laws Eq.(21) and Eq.(22), as well as Eq.(B.5) and Eq.(B.6) together with the definitions Eq.(27) - Eq.(30), into the free-energy imbalance Eq.(26), we obtain the local form of the free-energy imbalance:

$$\dot{\psi}_R \leq \mathbf{P}_{\mathrm{T}} : \dot{\mathbf{F}} + \boldsymbol{\Sigma} : \dot{\mathbf{H}} - \boldsymbol{\pi} \cdot \dot{\mathbf{n}} + \mathbf{e}_R \cdot \dot{\mathbf{d}}_R, \tag{31}$$

and the dissipation density with the property $\mathcal{D} \geq 0$,

$$\mathcal{D} = -\dot{\psi}_R + \mathbf{P}_{\mathrm{T}} : \dot{\mathbf{F}} + \boldsymbol{\Sigma} : \dot{\mathbf{H}} - \boldsymbol{\pi} \cdot \dot{\mathbf{n}} + \mathbf{e}_R \cdot \dot{\mathbf{d}}_R \geq 0. \tag{32}$$

To account for viscous dissipation in the presented model, specifically of the Kelvin–Voigt type represented by an additional damper in the generalized Maxwell model shown in Fig.3, the first Piola–Kirchhoff stress tensor is assumed to admit an additive decomposition into a viscous part $\mathbf{P}^{kv}$ and the remaining viscoelastic contribution $\mathbf{P}$ as follows:

$$\mathbf{P}_{\mathrm{T}} = \mathbf{P} + \mathbf{P}^{kv}. \tag{33}$$

According to $\mathbf{n} = \mathbf{R}\mathbf{n}_0$, where $\mathbf{R}$ is a proper orthogonal tensor satisfying $\mathbf{R}\mathbf{R}^T = \mathbf{I}$, the time derivatives of $\mathbf{n}$ and the second-order tensor $\mathbf{H}$ are given by:

$$\dot{\mathbf{n}} = \boldsymbol{\Omega}^R \mathbf{n} = \boldsymbol{\omega}^R \times \mathbf{n}, \quad \text{and} \quad \dot{\mathbf{H}} = \overline{\nabla \dot{\mathbf{n}}} = \boldsymbol{\Omega}^R \mathbf{H} - \mathbf{n} \nabla \boldsymbol{\Omega}^R, \tag{34}$$

where $\boldsymbol{\omega}^R$ denotes the angular velocity vector, which is the axial vector of the skew-symmetric tensor $\boldsymbol{\Omega}^R$ defined previously. By substituting Eq.(34) and Eq.(33) into Eq.(32), and using the relation Eq.(A.10), we obtain a new form of the dissipation density:

$$\mathcal{D} = -\dot{\psi}_R + \mathbf{P} : \dot{\mathbf{F}} + \mathbf{P}^{kv} : \dot{\mathbf{F}} - \boldsymbol{\Sigma} : \mathbf{n} \nabla \boldsymbol{\Omega}^R - \mathrm{skw} \boldsymbol{\tau}_{\mathrm{T}} : \boldsymbol{\Omega}^R + \mathbf{e}_R \cdot \dot{\mathbf{d}}_R \geq 0, \tag{35}$$

where $\boldsymbol{\tau}_{\mathrm{T}}$ is the total Kirchhoff stress tensor related to the the first Piola-Kirchhoff stress tensor $\mathbf{P}_{\mathrm{T}}$ through the relation $\boldsymbol{\tau}_{\mathrm{T}} = \mathbf{P}_{\mathrm{T}} \mathbf{F}^T$.

An alternative form of the dissipation density Eq.(32) can be obtained by expressing the axial vectors corresponding to the skew-symmetric tensors in the following form:

$$\mathrm{skw} \boldsymbol{\tau}_{\mathrm{T}} = -\boldsymbol{\varepsilon} \cdot \boldsymbol{\omega}^{\boldsymbol{\tau}}, \quad \text{and} \quad \boldsymbol{\Omega}^R = -\boldsymbol{\varepsilon} \cdot \boldsymbol{\omega}^{\mathbf{R}}, \tag{36}$$

where $\boldsymbol{\varepsilon}$ is the third-order permutation symbol, and the axial vectors $\boldsymbol{\omega}^{\boldsymbol{\tau}}$ and $\boldsymbol{\omega}^{\mathbf{R}}$ correspond to the skew-symmetric tensors $\mathrm{skw} \boldsymbol{\tau}_{\mathrm{T}}$ and $\boldsymbol{\Omega}^R$, respectively. Moreover, substituting the identity $\mathrm{skw} \boldsymbol{\tau}_{\mathrm{T}} : \boldsymbol{\Omega}^R = 2\boldsymbol{\omega}^{\boldsymbol{\tau}} \cdot \boldsymbol{\omega}^{\mathbf{R}}$ into Eq.(35), yields the final form of the dissipation density:

$$\mathcal{D} = -\dot{\psi}_R + \mathbf{P} : \dot{\mathbf{F}} + \mathbf{P}^{kv} : \dot{\mathbf{F}} - \boldsymbol{\Sigma} : \left(\mathbf{n} \times \nabla \boldsymbol{\omega}^{\mathbf{R}} \right) - 2\boldsymbol{\omega}^{\boldsymbol{\tau}} \cdot \boldsymbol{\omega}^{\mathbf{R}} + \mathbf{e}_R \cdot \dot{\mathbf{d}}_R \geq 0. \tag{37}$$

4.2. Reformulation of the stress-power

The general form of the stress power, expressed per unit reference volume, is given by [46]:

$$w_{int} = \mathbf{P} : \dot{\mathbf{F}} = \boldsymbol{\tau} : \mathbf{L}, \tag{38}$$

where the stress power is defined through stress–work conjugate pairs. To introduce the multi-branch generalized Maxwell model of viscoelasticity, we further decompose the stress power $\mathbf{P} : \dot{\mathbf{F}}$ associated with the stress tensor related to the steady state of the director rotation. Based on the multiplicative decomposition of the deformation gradient shown in Eq.(8) for the multi-branch viscoelastic model [55], and considering the additive decomposition of the Cauchy and Kirchhoff stress tensors, we have

$$\mathbf{T} = \sum_{i=0}^{M} \mathbf{T}^{(i)} \quad \text{and} \quad \boldsymbol{\tau} = \sum_{i=0}^{M} \boldsymbol{\tau}^{(i)}. \tag{39}$$

The next step is to redefine the stress-power term $\mathbf{P} : \dot{\mathbf{F}}$ appearing in the free-energy imbalance relation Eq.(35), by substituting Eq.(8), Eq.(9), Eq.(11), and Eq.(39), into the expression for the stress power:

$$\mathbf{P} : \dot{\mathbf{F}} = \sum_{i=0}^{M} \mathbf{S}^{e(i)} : \frac{1}{2}\dot{\mathbf{C}}^{e(i)} + \sum_{i=0}^{M} \mathbf{M}^{e(i)} : \mathbf{L}^{v(i)}. \tag{40}$$

where we can define the following stress measures: the elastic second Piola-Kirchhoff stress tensor

$$\mathbf{S}^{e(i)} = \mathrm{J}^{e(i)} \mathbf{F}^{e(i)-1} \mathbf{T}^{(i)} \mathbf{F}^{e(i)-T}, \tag{41}$$

and the elastic Mandel stress tensor

$$\mathbf{M}^{e(i)} = \mathbf{C}^{e(i)} \mathbf{S}^{e(i)}. \tag{42}$$

Within the present model, the stress power Eq.(40) is reformulated in terms of the Kirchhoff stress tensor. The expression is simplified by extracting the zero term from the summation and invoking $\mathbf{F}^{v(0)} = \mathbf{I}$, yielding

$$\boldsymbol{\tau} : \mathbf{L} = \boldsymbol{\tau}^{(0)} \mathbf{F}^{e(0)-T} : \dot{\mathbf{F}}^{e(0)} + \sum_{i=1}^{M} \boldsymbol{\tau}^{(i)} \mathbf{F}^{e(i)-T} : \dot{\mathbf{F}}^{e(i)} + \sum_{i=1}^{M} \mathbf{M}^{e(i)} : \mathbf{L}^{v(i)}, \tag{43}$$

and the elastic Mandel stress tensor as

$$\mathbf{M}^{e(i)} = \mathbf{F}^{e(i)T} \boldsymbol{\tau}^{(i)} \mathbf{F}^{e(i)-T}, \quad (i = 1, ..., M)\,. \tag{44}$$

The local form of the free-energy imbalance becomes

$$\mathcal{D} = -\dot{\psi_R} + \boldsymbol{\tau}^{(0)} \mathbf{F}^{e(0)-T} : \dot{\mathbf{F}}^{e(0)} + \sum_{i=1}^{M} \boldsymbol{\tau}^{(i)} \mathbf{F}^{e(i)-T} : \dot{\mathbf{F}}^{e(i)} + \sum_{i=1}^{M} \mathbf{M}^{e(i)} : \mathbf{L}^{v(i)} \tag{45}$$

$$+ \mathbf{P}^{kv} : \dot{\mathbf{F}} - \boldsymbol{\Sigma} : \mathbf{n} \nabla \boldsymbol{\Omega}^{R} - \mathrm{skw} \boldsymbol{\tau}_{\mathrm{T}} : \boldsymbol{\Omega}^{R} + \mathbf{e}_R \cdot \dot{\mathbf{d}}_R \geq 0.$$

5. The constitutive theory

5.1. The Coleman-Noll procedure

In the present work, the material model accounting for the dissipation effects in nematic LCEs is formulated through internal variables and their associated evolution equations. From a physical standpoint, these evolution equations must ensure a non-negative dissipation rate, as required by Eq.(45). By following the Coleman–Noll procedure, the constitutive relations for the Kirchhoff stress tensors, together with the evolution equations governing the internal variables associated with each viscoelastic branch, can be systematically derived from Eq.(45). This derivation is carried out under the assumption that the Helmholtz free energy density admits an additive decomposition over the individual branches of the generalized Maxwell model, i.e., as a sum of branch-wise free-energy contributions

$$\psi_R = \sum_i \psi_R^{(i)}(\mathbf{F}^{e(i)}, \mathbf{n}, \mathbf{H}, \mathbf{d}_R), \tag{46}$$

with the associated time derivative of the free energy density, considering Eq.(34), expressed as

$$\dot{\psi}_R = \frac{\partial \psi_R^{(0)}}{\partial \mathbf{F}^{e(0)}} : \dot{\mathbf{F}}^{e(0)} + \sum_{i=1}^{M} \frac{\partial \psi_R^{(i)}}{\partial \mathbf{F}^{e(i)}} : \dot{\mathbf{F}}^{e(i)} + \left[\frac{\partial \psi_R}{\partial \mathbf{n}} \otimes \mathbf{n} + \frac{\partial \psi_R}{\partial \mathbf{H}} \mathbf{H}^T \right] : \boldsymbol{\Omega}^R - \frac{\partial \psi_R}{\partial \mathbf{H}} : \left(\mathbf{n} \nabla \boldsymbol{\Omega}^R \right) + \frac{\partial \psi_R}{\partial \mathbf{d}_R} \cdot \dot{\mathbf{d}}_R. \quad (47)$$

Inserting Eq.(47) into Eq.(45) and applying the Coleman–Noll procedure, the following constitutive equations are obtained:

$$\boldsymbol{\tau}^{(i)} = \frac{\partial \psi_R^{(i)}}{\partial \mathbf{F}^{e(i)}} \mathbf{F}^{e(i)T}, \quad (48)$$

$$\mathrm{skw}\boldsymbol{\tau}_{\mathrm{T}} = -\mathrm{skw} \left[\frac{\partial \psi_R}{\partial \mathbf{n}} \otimes \mathbf{n} + \frac{\partial \psi_R}{\partial \mathbf{H}} \mathbf{H}^T \right], \quad (49)$$

$$\boldsymbol{\Sigma} = \frac{\partial \psi_R}{\partial \mathbf{H}}, \quad \boldsymbol{\pi} = -\frac{\partial \psi_R}{\partial \mathbf{n}}, \quad \mathbf{e}_R = \frac{\partial \psi_R}{\partial \mathbf{d}_R}. \quad (50)$$

The reduced dissipation inequality then reads as

$$\mathcal{D} = \sum_i \mathbf{M}^{e(i)} : \mathbf{L}^{v(i)} + \mathbf{P}^{kv} \mathbf{F}^T : \mathbf{L} \geq 0. \quad (51)$$

From this inequality, evolution equations for each branch of the generalized Maxwell model, corresponding to the viscous part of the strain tensor, can be derived. To satisfy Eq.(51), the following form for $\mathbf{L}^{v(i)}$ is assumed:

$$\mathbf{L}^{v(i)} = \frac{1}{\eta_N^{(i)}} \mathbf{M}^{e(i)}. \quad (52)$$

For the viscous Kirchhoff stress tensor $\boldsymbol{\tau}^{kv} = \mathbf{P}^{kv} \mathbf{F}^T$, associated with the Kelvin–Voigt dissipation added to the generalized Maxwell model [44], we assume

$$\boldsymbol{\tau}^{kv} = \eta_0 \mathrm{J} \mathbf{D}, \quad (53)$$

where $\mathbf{D}$ denotes the symmetric part of the velocity gradient tensor $\mathbf{L}$. Introducing Eq.(52) and Eq.(53) into inequality Eq.(51), the residual dissipation inequality reduces to

$$\boxed{\sum_i \eta_N^{(i)} \|\mathbf{L}^{v(i)}\|^2 + \eta_0 \mathrm{J} \|\mathbf{D}\|^2 \geq 0.} \quad (54)$$

Here, $\eta_N^{(i)} \geq 0$ are the network viscosity parameters associated with the dashpots of the generalized Maxwell model, while $\eta_0 \geq 0$ is the viscosity parameter corresponding to the additional Kelvin–Voigt dissipation. The norms $\|\mathbf{L}^{v(i)}\|$ and $\|\mathbf{D}\|$ denote the Frobenius norms of the viscous velocity gradient and strain rate tensors, respectively.

5.2. The Helmholtz free energy

In the presented model of the dielectric LCE, the Helmholtz free energy is decomposed into the mechanical, Frank, and electrical contributions, enabling a consistent description of the coupled electro-mechanical and orientation behavior of nematic micro-structures. The mechanical part, ψ_R^{Mech}, represents the response of the polymer network and consists of several physically distinct mechanisms. The equilibrium contribution, ψ_R^{EQ}, captures the elastic response associated with large, reversible deformations of the LCE, while the volumetric term, ψ_R^{Vol}, accounts for compressibility of the material. The non-equilibrium contribution, ψ_R^{NEQ}, reflects time-dependent and dissipative processes arising from internal relaxation mechanisms, which are essential for describing rate-dependent actuation behavior. The anisotropic contribution to the mechanical part of the free energy, ψ_R^{anis}, models the anisotropic elastic effects induced by the nematic microstructure. The adopted form of the Helmholtz free energy is based on the [37] with certain modifications in the anisotropic contribution in order to improve fitting of the experimental results that will be discussed later in the text.

The additive decomposition of the total Helmholtz free energy is applied as:

$$\psi_R = \psi_R^{Mech} + \psi_R^{Frank} + \psi_R^{Elec}, \quad (55)$$

where ψ_R^{Frank} is the Frank elastic energy and ψ_R^{Elec} is the electrostatic contribution to the total free energy.

The mechanical free energy contribution, composed of equilibrium, volumetric and non-equilibrium terms, and the one accounting for the anisotropic elastic effects, i.e.

$$\psi_R^{Mech} = \psi_R^{EQ} + \psi_R^{Vol} + \psi_R^{NEQ} + \psi_R^{anis}, \tag{56}$$

$$\psi_R^{EQ} = \underbrace{\frac{1}{2}\mu_0^{EQ}\left(\mathrm{tr}\overline{\mathbf{K}} - 3\right) + \mu_a^{EQ}\left(\mathrm{tr}\overline{\mathbf{K}} - 3\right)^2 + \frac{1}{2}\mu_0^{EQ}\overline{a}\|\overline{\mathbf{n}}_{\overline{\mathbf{F}}}\|^2}_{\text{equilibrium energy}}, \tag{57}$$

$$\psi_R^{Vol} = \underbrace{\frac{1}{2}K(\mathrm{J}-1)^2}_{\text{volumetric energy}}, \tag{58}$$

$$\psi_R^{NEQ} = \sum_i \underbrace{\frac{1}{2}\mu_{(i)}^{NEQ}\left[\left(\mathrm{tr}\overline{\mathbf{K}}^{e(i)} - 3\right) + 2\frac{\mu_a^{EQ}}{\mu_0^{EQ}}\left(\mathrm{tr}\overline{\mathbf{K}}^{e(i)} - 3\right)^2\right] + \frac{1}{2}\mu_{(i)}^{NEQ}\overline{a}_{(i)}\|\overline{\mathbf{n}}_{\overline{\mathbf{F}}^{e(i)}}\|^2}_{\text{non-equilibrium energy}}, \tag{59}$$

$$\psi_R^{anis} = \underbrace{\frac{k_1}{2k_2}\left(\exp\left[k_2(\overline{I}_4 - 1)^2 - 1\right]\right)}_{\text{anisotropic energy}}, \tag{60}$$

where we define two additional isochoric tensors as

$$\overline{\mathbf{K}} = \mathbf{l}^{-1}\overline{\mathbf{F}}\mathbf{l}_0\overline{\mathbf{F}}^T \quad \text{and} \quad \overline{\mathbf{K}}^{e(i)} = \mathbf{l}^{-1}\overline{\mathbf{F}}^{e(i)}\mathbf{l}_0\overline{\mathbf{F}}^{e(i)T}, \tag{61}$$

in which μ_0^{EQ} and $\mu_{(i)}^{NEQ}$ are related to the equilibrium and non-equilibrium shear moduli for the i-th branch, K is the bulk modulus and μ_a^{EQ} is the elasticity coefficient proposed in [37]. The mechanical free energy should also account for the anisotropy of the material introduced by the presence of mesogens. In a manner similar to modeling of the material anisotropy of fiber-reinforced materials, this anisotropic contribution to the mechanical free energy is represented by the isochoric invariant defined as $\overline{I}_4 = \overline{\mathbf{C}} : \mathbf{n}_0 \otimes \mathbf{n}_0$. This contribution involves two material parameters: the stress-like parameter k_1 and the dimensionless parameter k_2, which can be determined experimentally, as proposed in [65]. The strain-energy function adopted in this study represents a simplified example commonly used to describe the mechanical behavior of LCEs. However, more sophisticated forms of strain-energy functions may be employed to account for additional material nonlinearities and complex physical effects. A fundamental modification of the Helmholtz free energy, accounting for the combined mechanical, nematic, and volumetric contributions, is introduced by assuming that the material is nearly incompressible. Accordingly, the total deformation gradient is replaced by its isochoric part. As a consequence, the resulting stress tensors are defined solely in terms of the deviatoric parts of the strain measures, which also incorporate the effects of nematic anisotropy. Further details on the frame indifference and objectivity of the Helmholtz free energy employed for LCEs can be found in [27, 36].

Moreover, we define dimensionless shape tensors in the current and initial configurations, incorporating the nematic director field as

$$\mathbf{l} = r_\perp\left[\mathbf{I} + (r-1)\,\mathbf{n}\otimes\mathbf{n}\right], \quad \mathbf{l}_0 = r_\perp\left[\mathbf{I} + (r-1)\,\mathbf{n}_0\otimes\mathbf{n}_0\right], \tag{62}$$

and its inverse as

$$\mathbf{l}^{-1} = r_\perp^{-1}\mathbf{I} + k\mathbf{n}\otimes\mathbf{n}, \quad \text{and} \quad k = r_\perp^{-1}\left(r^{-1} - 1\right),$$

where $r = \frac{r_\parallel}{r_\perp}$ is the shape anisotropy of the mesogen orientation, i.e. the *nematic anisotropy* as defined in [24], while $\mathbf{n}_0$ is the initial director. This nematic anisotropy should be differed from the above introduced material anisotropy, which is a macroscopic material feature. In general, according to the monographic study mentioned above, it is stated that the most important parameter in Eq.(62) is the shape anisotropy of the chain distribution $(r_\parallel - r_\perp)$. Moreover, it can also be assumed that the fractional anisotropy $(r-1)$ is proportional to the nematic order parameter Q and in this way all the principal features of nematic elastomers can be determined. The step lengths, along the director $r_\parallel$ and in the perpendicular plane $r_\perp$, determine the anisotropy and relations with order parameter Q, with nematic anisotropy ratio $r = \frac{r_\parallel}{r_\perp} = (1+2Q)/(1-Q)$. The quantity Q is a directly measurable in experiments by X-ray scattering testing [24].

The term given in $\frac{1}{2}\mu_0^{EQ}\overline{a}\|\overline{\mathbf{n}}_{\overline{\mathbf{F}}}\|^2$ characterizes the non-ideal part due to varying chain anisotropy, where $\overline{a}$ is the semi-soft parameter indicating the degree of these variations, which can be defined as

$$\|\overline{\mathbf{n}}_{\overline{\mathbf{F}}}\|^2 = \mathrm{tr}\left[(\mathbf{n}\otimes\mathbf{n})\,\overline{\mathbf{F}}\,(\mathbf{I}-\mathbf{n}_0\otimes\mathbf{n}_0)\,\overline{\mathbf{F}}^T\right], \tag{63}$$

According to [37], we can assume that the parameter $\overline{a}$ depends on the isochoric part of the deformation gradient $\overline{\mathbf{F}}$,

$$\overline{a} = \overline{a}_t + a_p = \frac{a_0}{m\left[\mathrm{tr}(\overline{\mathbf{F}}^T\overline{\mathbf{F}}) - 3\right] + 1} + a_p, \tag{64}$$

where a_p and a_0 are constants, and $\overline{a}_t$ is the transient part of the semi-soft parameter. On the other hand, the non-equilibrium counterpart of these semi-soft effects is determined as

$$\|\overline{\mathbf{n}}_{\overline{\mathbf{F}}^{e(i)}}\|^2 = \mathrm{tr}\left[(\mathbf{n}\otimes\mathbf{n})\,\overline{\mathbf{F}}^{e(i)}\,(\mathbf{I}-\mathbf{n}_0\otimes\mathbf{n}_0)\,\overline{\mathbf{F}}^{e(i)T}\right], \tag{65}$$

and

$$\overline{a}_{(i)} = \overline{a}_{t(i)} + a_p = \frac{a_0}{m\left[\mathrm{tr}(\overline{\mathbf{F}}^{e(i)T}\overline{\mathbf{F}}^{e(i)}) - 3\right] + 1} + a_p. \tag{66}$$

The second term in the free energy formulation Eq.(55) corresponds to the Frank elastic energy, which accounts for scale-dependent effects related to the gradient of the nematic director field,

$$\psi_R^{Frank} = \frac{\mathrm{J}K_F}{2}\|\mathrm{grad}\mathbf{n}\|^2 = \frac{\mathrm{J}K_F}{2}\|(\nabla\mathbf{n})\,\mathbf{F}^{-1}\|^2, \tag{67}$$

where K_F is the Frank constant. The Frank contribution, ψ_R^{Frank}, penalizes spatial distortions of the nematic director field and governs director reorientation and stability under mechanical and electrical loading.

The last contribution to the Helmholtz free energy density in Eq.(55) corresponds to the electric free energy given as

$$\psi_R^{Elec} = \frac{\mathrm{J}}{2}\mathbf{d}\cdot\mathbf{e} = \frac{1}{2\mathrm{J}}\mathbb{D}_n^{-1} : (\mathbf{F}\mathbf{d}_R\otimes\mathbf{F}\mathbf{d}_R), \tag{68}$$

in which the inverse dielectric tensor is defined as

$$\mathbb{D}_n^{-1} = \tilde{\varepsilon}\mathbf{n}\otimes\mathbf{n} + \varepsilon_a^{-1}\mathbf{I} \quad \text{and} \quad \tilde{\varepsilon} = \frac{\varepsilon_a - \varepsilon_c}{\varepsilon_a\varepsilon_c}. \tag{69}$$

where we use the relationship between vector of electric field and electric displacement in the form which is given in Eq.(B.4). The electrical contribution ψ_R^{Elec}, characterizes the interaction between the applied electric field and the dielectric anisotropy of the LCE, serving as the primary driving mechanism for electrically induced actuation. Together, these contributions form a comprehensive energetic framework for modeling deformation, director evolution, and electro-mechanical coupling in dielectric LCE actuators.

In **Appendix C**, detailed derivations are provided concerning the constitutive relations, including the stress tensor, along with the remaining constitutive relations.

5.3. Evolution equations

Considering the dissipation inequality given in Eq.(51), the evolution equations for the viscous deformation can be derived to ensure that this inequality is satisfied. These evolution equations correspond to the non-equilibrium branch and are associated with dissipation mechanisms within the polymer network.

In the framework of finite viscoelasticity, recent studies such as Ricker et al. [66] and Stewart and Anand [55] propose neglecting the viscous spin tensor $\mathbf{W}^{v(i)}$ associated with the non-equilibrium (viscous) branches. This simplification is motivated by experimental observations and theoretical arguments for certain classes of polymeric materials, where the spin contribution is assumed negligible in the overall dissipation. However, the present formulation retains the full viscous portion of the velocity gradient without assuming or explicitly neglecting the viscous spin tensor components $\mathbf{W}^{v(i)}$. From Eq.(54), it is straightforward to derive the evolution equations for the viscous part of the deformation gradient, $\dot{\mathbf{F}}^{v(i)} = \mathbf{L}^{v(i)}\mathbf{F}^{v(i)}$,

$$\dot{\mathbf{F}}^{v(i)} = \frac{1}{\eta_N^{(i)}}\mathbf{M}^{e(i)}\mathbf{F}^{v(i)}. \tag{70}$$

Introducing Eq.(44) and Eq.(C.9) into Eq.(70), and after some algebraic manipulation, we obtain the final form of the evolution equation as

$$\boxed{\dot{\mathbf{F}}^{v(i)} = \frac{1}{\tau_r^{(i)}} \mathbf{F}^{v(i)-T} \mathbf{F}^T \left[-\overline{g}_0^{e(i)} \overline{\mathbf{K}}_0^{e(i)} - \left(\frac{m}{a_0} \right) \| \overline{\mathbf{n}}_{\overline{\mathbf{F}}^{e(i)}} \|^2 \overline{a}_{t(i)}^2 \overline{\mathbf{B}}_0^{e(i)} + \overline{a}_{(i)} \overline{\mathbf{Z}}_0^{e(i)} \right] \mathbf{F}^{-T} \mathbf{C}^{v(i)}.} \tag{71}$$

Here, we define the relaxation time for the i-th branch as $\tau_r^{(i)} = \frac{\eta_N^{(i)}}{\mu_{(i)}^{NEQ}}$. The total number of the evolution equations is related to the number of branches in the generalized Maxwell's material model. It should be noted that for the numerical implementation of the evolution equations, one needs to introduce the relation $\mathbf{F}^{e(i)} = \mathbf{F}\mathbf{F}^{v(i)-1}$.

6. Summary of the governing equations and evolution equations

6.1. Equations of motion

Here, we provide a concise summary of the derived governing partial differential equations and evolution equations describing the electro-viscoelastic behavior of nematic LCEs. These governing and evolution equations will be implemented in the FEniCSx environment through the formulation of their corresponding weak forms, enabling efficient numerical simulation and analysis of the model [67, 68].

Within the scope of the present work, the analysis is restricted to plane stress and plane strain regimes. Consequently, the initial plane in which the directors rotate remains fixed, allowing the director field $\mathbf{n}$ to be conveniently parameterized by a single variable, as the angle of mesogen rotation θ. Under these assumptions, it is not necessary to introduce additional Lagrange multipliers to enforce the inextensibility constraint of the director during deformation. Furthermore, since the material is modeled as nearly incompressible, the volumetric constraint can be effectively enforced by assigning a sufficiently large value to the bulk modulus K. This penalty-type approach eliminates the need to impose incompressibility explicitly through additional constraints. The orientational balance law has been reduced accordingly, and the details of this reduction are provided in **Appendix D**. Therefore, only the resulting reduced form, suitable for the two-dimensional setting, is presented here.

The presented electro-viscoelastic model of the nematic LCEs, is based on the following set of equations:

- The balance law for linear momentum:

$$\mathrm{Div}\mathbf{P}_{\mathrm{T}} + \mathbf{b}_R = \mathbf{0}. \tag{72}$$

- The balance law for orientation momentum in reduced form:

$$\mathrm{Div}\boldsymbol{\sigma}^{Frank} + h = 0, \tag{73}$$

- Gauss's law for electrostatics:

$$\mathrm{Div}\mathbf{d}_R = 0. \tag{74}$$

- The evolution equation for viscous part of the deformation gradient:

$$\dot{\mathbf{F}}^{v(i)} = \frac{1}{\tau_r^{(i)}} \mathbf{F}^{v(i)-T} \mathbf{F}^T \left[\overline{g}_0^{e(i)} \overline{\mathbf{K}}_0^{e(i)} - \left(\frac{m}{a_0} \right) \| \overline{\mathbf{n}}_{\overline{\mathbf{F}}^{e(i)}} \|^2 \overline{a}_{t(i)}^2 \overline{\mathbf{B}}_0^{e(i)} + \overline{a}_{(i)} \overline{\mathbf{Z}}_0^{e(i)} \right] \mathbf{F}^{-T} \mathbf{C}^{v(i)}. \tag{75}$$

It should be noted that, in the following numerical examples, the orientational momentum is employed in its reduced form, as presented in **Appendix D** (see Eq.(D.4)).

6.2. Stress tensor and vectors

The total first Piola–Kirchhoff stress tensor is given by,

$$\mathbf{P}_{\mathrm{T}} = \mathbf{P} + \mathbf{P}^{kv} = \mathbf{P}^{EQ} + \mathbf{P}^{anis} + \mathbf{P}^{NEQ} + \mathbf{P}^{Frank} + \mathbf{P}^{MW} + \mathbf{P}^{kv}, \tag{76}$$

where the stress contributions include the equilibrium and non-equilibrium mechanical stresses, the Frank elastic stress, the Maxwell stress, and the Kelvin–Voigt-type dissipative stress. The reduced orientational stress tensor is defined as

$$\boldsymbol{\sigma}^{Frank} = \mathrm{J} K_F \mathbf{F}^{-1} \mathbf{F}^{-T} \nabla\theta, \tag{77}$$

The internal director body force is taken in the reduced form as

$$h = -\left(\mathbf{m}^{EQ} + \mathbf{m}^{NEQ} + \mathbf{m}^{Frank} + \mathbf{m}^{Elec}\right) \cdot \mathbf{Un}. \tag{78}$$

The electric displacement vector in the reference configuration is given by

$$\mathbf{d}_R = \mathrm{J}\mathbf{F}^{-1}\mathbb{D}_n\mathbf{F}^{-T}\mathbf{e}_R. \tag{79}$$

6.3. Boundary and initial conditions

To complete the modeling process, the appropriate initial and boundary conditions have to be specified for the governing equations Eq.(72)–Eq.(75), along with the initial conditions for the evolution equations. These conditions are essential for the subsequent analysis.

- **Mechanical boundary conditions**
  To define mechanical boundary conditions we need to prescribe the displacement $\overline{\mathbf{u}}$ and traction force $\overline{\mathbf{t}}_R$, in time interval $t \in [0, T]$ on boundary surfaces $\partial\mathcal{B}_{\mathbf{u}}$ and $\partial\mathcal{B}_{\mathbf{t}_R}$ of the body $\mathcal{B}$,

$$\mathbf{u} = \overline{\mathbf{u}}, \quad \text{on} \quad \partial\mathcal{B}_{\mathbf{u}} \times [0, T], \tag{80}$$

$$\mathbf{P}_{\mathrm{T}}\boldsymbol{\nu}_R = \overline{\mathbf{t}}_R, \quad \text{on} \quad \partial\mathcal{B}_{\mathbf{t}_R} \times [0, T].$$

- **Electric boundary conditions**
  To define electrical boundary conditions we need to prescribe electrostatic potential $\overline{\phi}$ and electric displacement $\overline{\mathbf{d}}_R$, in time interval $t \in [0, T]$ on boundary surfaces $\partial\mathcal{B}_{\phi}$ and $\partial\mathcal{B}_{\mathbf{d}_R}$ of the body $\mathcal{B}$,

$$\phi = \overline{\phi}, \quad \text{on} \quad \partial\mathcal{B}_{\phi} \times [0, T], \tag{81}$$

$$\omega_R = -\overline{\mathbf{d}}_R\boldsymbol{\nu}_R, \quad \text{on} \quad \partial\mathcal{B}_{\mathbf{d}_R} \times [0, T].$$

- **Director boundary conditions**
  To define nematic boundary conditions we need to prescribe initial values for $\overline{\theta}$ and $\overline{m}_\theta$ on the boundary surface $\partial\mathcal{B}_\theta$ and $\partial\mathcal{B}_{m_\theta}$ of the body $\mathcal{B}$,

$$\theta = \overline{\theta}, \quad \text{on} \quad \partial\mathcal{B}_\theta \times [0, T], \tag{82}$$

$$m_\theta = \overline{m}_\theta, \quad \text{on} \quad \partial\mathcal{B}_{m_\theta} \times [0, T].$$

  In all numerical examples presented in this analysis, we adopt the following value $\overline{m}_\theta = 0$.

- **Initial conditions**
  To fully specify the initial value problem, it is necessary to prescribe the corresponding initial condition functions over the body $\mathcal{B}$, providing the required initial distributions of relevant physical fields,
  - Displacement and velocities: $\mathbf{u}(\mathbf{X}, 0) = \mathbf{u}_0(\mathbf{X})$, and $\mathbf{v}(\mathbf{X}, 0) = \mathbf{v}_0(\mathbf{X})$,
  - Electric field: $\phi(\mathbf{X}, 0) = \phi_0(\mathbf{X})$,
  - Director field: $\theta(\mathbf{X}, 0) = \theta_0(\mathbf{X})$,
  - Viscous deformation: $\mathbf{F}^{v(i)}(\mathbf{X}, 0) = \mathbf{I}$ in $\mathcal{B}$.

7. Numerical results

This section presents the development of an accurate and efficient computational framework for simulating rate-dependent, nonlinear viscoelastic responses of nematic LCEs under uniaxial tension, electro-mechanical bending and buckling. The model is first validated against the experimental data for different values of strain rates and initial director orientation. Finite element method is used for spatial discretization, while the time integration was done by using the backward Euler scheme. This numerical approach is well-suited for capturing the intricate electro-mechanical coupling characteristic of dielectric LCEs, enabling a detailed analysis under various boundary conditions and internal constraints. The weak form equations, given in **Appendix E**, are implemented in the open-source FEniCSx platform, allowing for the simulation of large deformations, internal microstructural reorganization, and field-induced actuation. Visualization is

performed in ParaView software. The results provide valuable insights into the complex behavior of dielectric LCEs and confirm the accuracy and predictive capability of the presented theoretical model. It should also be mentioned that all the cases considered in this section represent 2D problems, the validation study was done for a plane-stress assumption, while all the subsequent simulations analyzing electro-mechanical deformation and buckling, were done for the plane-strain formulation.

It is important to note that director rotation occurs only if a specific condition is satisfied. As shown in [20], when the dielectric anisotropy r_ϵ (see **Appendix B**) exceeds the value of the shape anisotropy r, i.e., $r/r_\epsilon < 1$, the nematic directors rotate toward the direction of the applied electric field. During the electric Fréedericksz transition in a dielectric LCE block, different electro-mechanical deformation modes may develop. These modes are typically localized and strongly nonlinear, which makes analytical treatment challenging. For instance, when an electric potential is applied to a bi-layer dielectric LCE with a nematic microstructure, bulk instabilities such as buckling may occur due to partial actuation, material anisotropy, and boundary conditions. In this work, a computational approach is used to investigate these instabilities in the viscoelastic regime. The configurations considered include bending of a fixed–free and buckling of a fixed-fixed bi-layer beam-lke 2D solid under different ramp rates of the applied electric potential, and the quasi-static evolution of deformation under uniaxial tension. When the nematic directors are initially aligned in the direction normal to the applied electric field and no director rotation occurs, the dielectric LCE behaves similarly to a classical DE, and the pull-in instability criterion coincides with that of standard DEs [20]. However, in conventional DEs the response changes significantly when viscoelastic effects are taken into account, since rate-dependent behavior strongly influences the onset of pull-in [69]. Similarly, the problem becomes more complex when director rotation precedes the uniform thinning induced by Maxwell stresses, particularly in the presence of viscoelasticity. For these reasons, the derivation of the pull-in instability criterion is beyond the scope of the present work.

In all the presented analyses, a mixed finite element method is employed, where the primary unknowns are the displacement vector $\mathbf{u}$, the rotation angle of the mesogens θ, the electrostatic field ϕ, the hydrostatic pressure p, and the viscous part of the deformation gradient $\mathbf{F}^{v(i)}$. For the presented numerical model of the dielectric LCE, these field variables $\mathbf{u}$, ϕ and p, and internal variables θ and $\mathbf{F}^{v(i)}$ are solved simultaneously at each time step, where the final number of varibales depend on the number of evolution equations. The adopted model represents a plane-strain reduction of the full three-dimensional formulation developed for a nematic LCE, where the initial orientation of the nematic microstructure is defined by the director $\mathbf{n}_0$. The LCE solid-beam is assumed to be equipped with two compliant electrodes, one bonded to the top surface and the other to the bottom surface, for the analysis of the electric Fréedericksz transition. In this configuration, only the vertical displacement at the bottom surface is constrained (Fig.4). For the analysis of bending and electrically induced buckling instability, the top compliant electrode remains on the upper surface, while the second electrode is embedded in the mid-plane of the solid-beam. For the bending analysis, a fixed boundary condition is imposed on the left side (Fig.4b), whereas for the buckling analysis fixed boundary conditions are applied on both lateral sides of the LCE sample (Fig.4c). It is important to emphasize that the compliant electrodes are assumed not to affect the mechanical stiffness of the system; therefore, their stiffness contribution is not incorporated into the electro-mechanical model of the nematic LCE.

The geometrical dimensions of the model used in simulations are provided in the subsequent analysis. In the following text, the measuring point for all the stretch diagrams is $0.5L_x$ and $0.5L_y$ while for the director angle we take $0.5L_x$ and $0.75L_y$ due to the director rotation in the case of a bi-layer sample, in which L_x and L_y are length and width of the LCE sample. All relevant parameter values and other important details will be provided for each considered case.

The source codes for the simulations reported in this Section are available online in the following GitHub repository: https://github.com/Caja84/Rate-dependent_electro-mechanical_deformation_LCE.

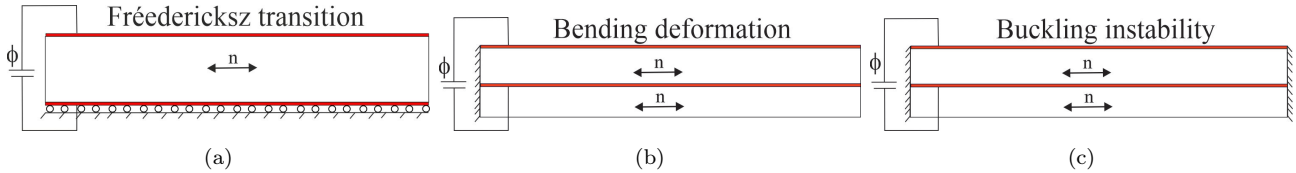

Figure 4: Schematic representation of a nematic LCE actuator with compliant electrodes (shown as thick red lines), together with the corresponding boundary conditions and the applied electric loading for three cases: (a) a single-layer actuator undergoing the Fréedericksz transition, (b) a bi-layer cantilever solid-beam for bending deformation analysis, and (c) a bi-layer solid-beam with fixed ends for buckling analysis.

7.1. Uniaxial tension

First, the validation study is performed by comparing our numerical results, obtained with the model presented above, against the experimental results for rate-dependent uniaxial tension of LCE samples found in the literature [37, 39]. The material model of the nematic LCE adopted for this analysis is based on the modified semi-soft free energy density function for both equilibrium and non-equilibrium branches, with the corresponding material parameters determined from uniaxial tension tests on LCE specimens. The parameters used in the validation study are summarized in Table 1 and Table 2. Most of the viscoelastic model parameters values were adopted from the referenced paper, while the anisotropic parameters k_1 and k_2 are applied in a manner consistent with [70]. The bulk modulus K is taken as $K = 1000\mu_0^{EQ}$.

Table 1: Geometrical and equilibrium material parameters.

μ_0^{EQ}[MPa]	k_1[MPa]	k_2	r	K_f[J/m^2]	a_0	a_p	m	ϵ_a	ϵ_c	L_x[mm]	L_y[mm]
0.7	0.44	0.1	5.5	10^{-11}	0.075	0.0	0.3	$7\epsilon_0$	$18.5\epsilon_0$	15.0	3.0

Table 2: Non-equilibrium parameters for the Maxwell's viscoelastic model.

i	1	2	3	4	5	6
τ_i [s]	0.2	1.0	6.0	42.0	336.0	2500.0
$\mu_{(i)}^{NEQ}/\mu_0^{EQ}$	7.206	4.164	2.288	1.047	0.648	0.409

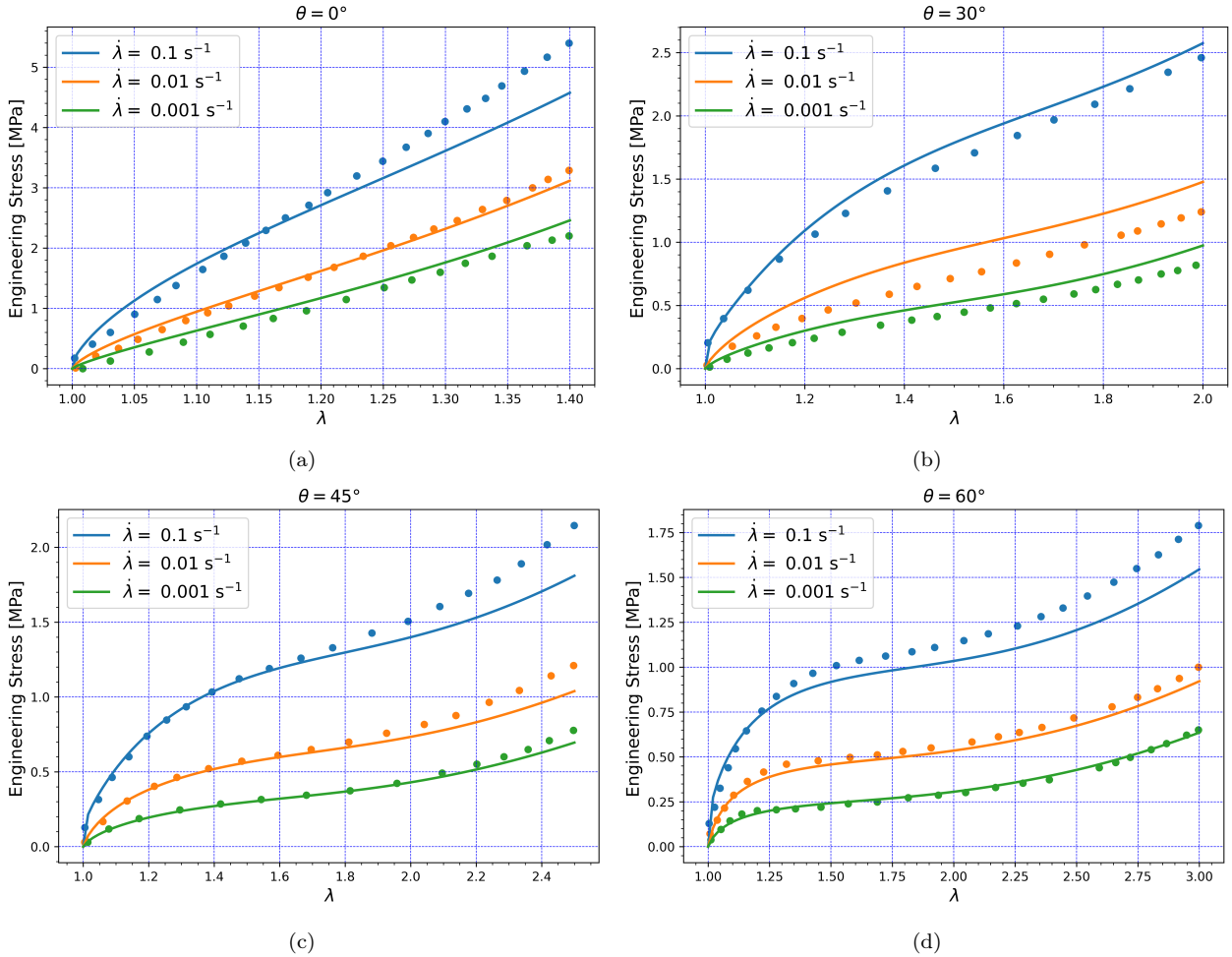

Figure 5: Validation of the numerical model against the experimental data for uniaxial tension of a nematic LCE, as reported by Wei et al. [39]. The comparison shows the numerical results (solid lines) and experimental measurements (dotted lines) for four initial orientations of the nematic director field: (a) $\theta_0 = 0°$, (b) $\theta_0 = 30°$, (c) $\theta_0 = 45°$ and (d) $\theta_0 = 60°$.

This loading scenario involves uniaxial tension, where an engineering strain is applied in a constant rate along the axial direction of the specimen. One end of the sample is fixed by prescribing the displacement field as $\mathbf{u} = \mathbf{0}$, while the stretch is induced by imposing the displacement at the opposite end, at a constant rate $\dot{\lambda}$, which represents the rate of change of the specimen's length relative to its initial length per unit time. The initial orientation of the nematic director field, $\mathbf{n}_0$, is defined relative to the x-axis and is specified by the angle between the director and this axis.

The resulting uniaxial stress response curves are presented in Fig.5, where the numerical predictions are compared against experimental data from the literature [39] for various strain rates and initial director orientations. The comparison shows good agreement and highlights a significant influence of both the strain rate and the director alignment on the uniaxial response of the nematic LCE. In the present study, six Maxwell branches were employed, each with distinct relaxation times and non-equilibrium shear moduli, along with an additional Kelvin–Voigt-type viscous dissipation term proportional to the strain-rate tensor. The figures present uniaxial tests performed for different initial director orientations, $\theta_0 = 0°, 30°, 45°, 60°$, and for different strain rates, $\dot{\lambda} = 0.1, 0.01, 0.001\,[\mathrm{s}^{-1}]$.

Fig.5 illustrates the semi-soft elasticity effect and viscoelastic characteristics of nematic elastomers, which are directly associated with the microstructural behavior of mesogens capable of rotating under mechanical deformation and with dissipation mechanisms in the polymer network. The general stress–strain response can be divided into three distinct regions: (i) *Initial elastic regime* — corresponding to the classical behavior of conventional elastomers, where stress increases monotonically with strain due to the stretching of the polymer network; (ii) *Semi-soft elasticity* — where a substantial increase in strain results in only a modest increase in stress, primarily due to internal reorientation of mesogens along the direction of maximum stretch. In this regime, deformation energy is mainly expended by the reordering of the internal structure, rather than by further elastic stretching of the network; and (iii) *Strain-stiffening regime* — where, once the mesogens are fully aligned, additional deformation leads to a renewed and significant increase in stress with strain, reflecting the intrinsic stiffening as both the polymer chains and mesogens are further stretched. Experimental evidence suggest that the manifestation of semi-soft elasticity and the transitions between these regimes are strongly influenced by the applied strain rate and the initial orientation angle θ_0 of the LC mesogens. Notably, higher values of θ_0 enhance the prominence of the semi-soft elasticity effect. Numerical results across all three cases for various strain rates also confirm that this effect is highly sensitive to the initial director orientation. In general, engineering stress increases with higher strain rates, whereas at lower strain rates, viscoelastic effects become more pronounced and significantly influence the mechanical response, resulting in much lower stresses throughout the entire deformation range. Although a noticeable discrepancy exists between the model predictions and the experimental results for the initial director orientations $\theta_0 = 0°$ and $30°$, the deviation remains within acceptable limits. Furthermore, the present model incorporates material anisotropy, which substantially enhances the accuracy of stress predictions at lower director inclination angles.

7.2. Fréedericksz transition and uniform thinning

For the results presented in this section, we adopted the following sample dimensions: $L_x = 0.34\,[\mathrm{mm}]$ and length to thickness ratio $L_x/L_y = 10$. Unless otherwise specified in the figures, we use the anisotropic step-length ratio $r = 1.5$ and the initial director angle $\theta_0 = 5°$. The other parameters remain the same as in the validation study. In general, the electric Fréedericksz transition is one of the fundamental electro-mechanical phenomena observed in electrically actuated nematic LCEs and LCs materials. From a physical standpoint, when a voltage difference is applied across the compliant electrodes, the nematic director tends to align with the direction of the applied electric field. During the Fréedericksz transition, the dimensions of the LCE solid-beam typically change, resulting in an expansion along the thickness direction. This behavior arises from the interaction between the electric field, LC mesogens and the polymer network of the elastomer. The boundary conditions, under which the fundamental deformation modes are analyzed during the electric Fréedericksz transition of the finite LCE solid-beam, assume that displacements at the bottom surface are constrained in the vertical direction. The remaining surfaces are free, i.e., no displacement constraints are imposed. In order to facilitate the specification of both the electric potential and the electric potential ramp rates for all cases where the rate plays a crucial role, we introduce a normalized electric potential defined as: $\tilde{\phi} = \frac{\phi}{L_y}\sqrt{\frac{\epsilon_a}{\mu_0^{EQ}}}$.

In the present analysis, we consider a two-dimensional, finite, solid-like LCE beam featuring a homogeneously distributed nematic director field $\mathbf{n}_0$, with its initial orientation defined by the angle θ_0. The director is initially aligned along the x-axis, upon which a small perturbation is superimposed. Fig.6 illustrates the

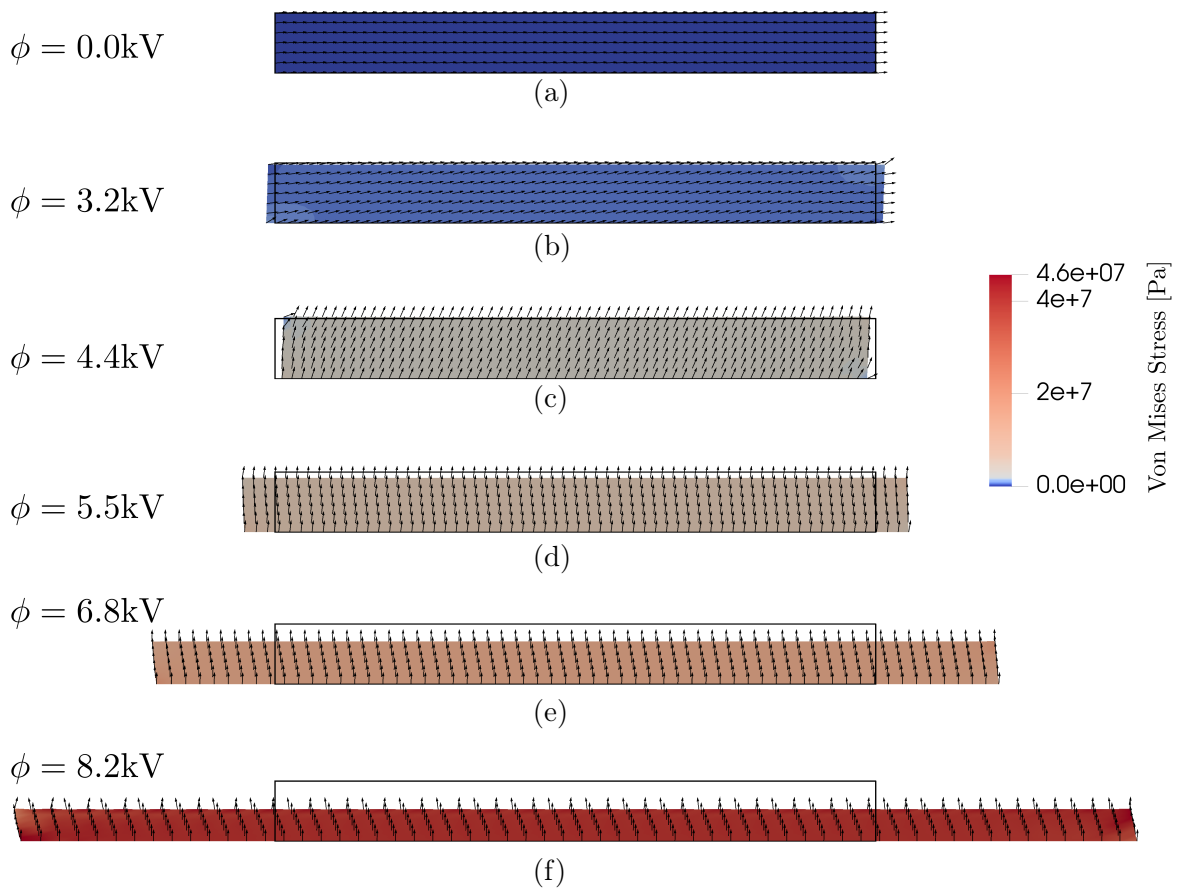

Figure 6: Snapshots from a quasi-static simulation showing the finite electro-viscoelastic response of a 2D free-standing nematic LCE block with electrodes applied to the top and bottom surfaces. The simulation illustrates the electric Fréedericksz transition and subsequent uniform thinning due to director field reorientation under an incrementally applied voltage up to 8.2 kV with electrical potential ramp rate $\dot{\phi} = 1.0$, for $r = 1.5$ and $\theta_0 = 5°$. The length to thickness ratio is adopted as $L_x/L_y = 10$. (a) The nematic LCE sample, initially featuring a uniform director field, is subjected to an electrostatic field. (b) At low voltage values, the LCE sample behaves like a classical DE until a critical electric potential is reached, at which point the director field begins to reorient in response to the applied voltage. (c) During the Fréedericksz transition, the directors align with the electric field, resulting in a contraction in the length direction. (d)-(f) Beyond the transition, further voltage increase leads to dominant Maxwell stress, causing contraction in the thickness direction through uniform thinning.

finite LCE rectangular block with two compliant electrodes, one attached to the top surface and the other to the bottom surface of the sample (Fig.6a). When a voltage difference ϕ is applied across the electrodes, the resulting electric field induces a reorientation of the nematic directors along the direction of the electric field (Fig.6b). During the ensuing electric Fréedericksz transition, this reorientation leads to an expansion in the thickness direction accompanied by a contraction along the solid-beam length (Fig.6c). Upon completion of the Fréedericksz transition, a continued increase in the electric potential leads to a significant increase of the Maxwell's stress, which exerts a compressive force on the LCE block along the thickness direction (Fig.6d). As the material thins under the applied electrostatic load (Fig.6e and f), a critical threshold may be reached beyond which the structure can no longer sustain the induced stress. This condition may result in localized thinning and the onset of pull-in instability, analogous to phenomena commonly observed in classical DE systems [9, 71, 72]. In general, inhomogeneities in the microstructure, the elastomeric matrix, or the applied electric field can induce localized deformations within the nematic elastomer. This localized thinning may, in turn, trigger a pull-in instability at a critical threshold, which can differ depending on the specific class of dielectric elastomer or dielectric LCE. However, such instabilities are not addressed in the present study for the reasons outlined above.

Fig.7a shows the electric Fréedericksz transition in a solid block of nematic LCE material for different initial orientation angles θ_0. As the initial angle of the nematic microstructural orientation increases from $\theta_0 = 5°$ to $\theta_0 = 60°$, it can be observed that the threshold voltage decreases significantly. It is worth noting that once the threshold voltage is reached, a large rotation of the directors occurs within a very narrow

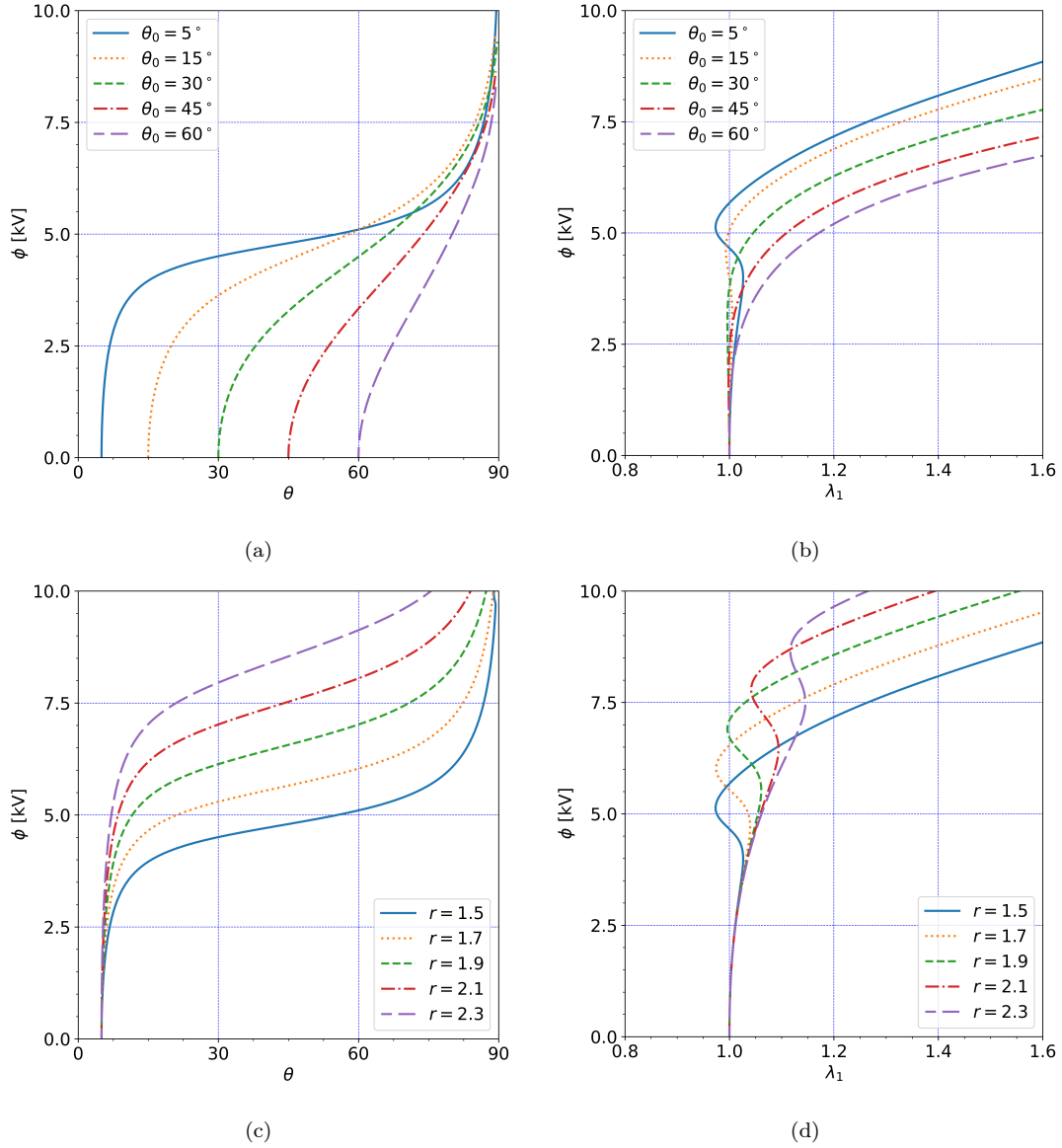

Figure 7: Demonstration of the electric Fréedericksz transition phenomenon through: (a) Relationship between the applied voltage and the rotation angle of the director field θ for different initial director orientation angles θ_0 and $r = 1.5$; (b) Relationship between the applied voltage and and the stretch λ_1 for different initial director orientation angles θ_0 and $r = 1.5$; (c) Relationship between the applied voltage and the director field θ for different values of the anisotropic step-length ratio r and $\theta_0 = 5°$; (d) Relationship between the applied voltage and the stretch λ_1 for different values of the anisotropic step-length ratio r and $\theta_0 = 5°$. The length to thickness ratio is adopted as $L_x/L_y = 10$.

voltage range; that is, the mesogen reorientation proceeds much more rapidly compared to cases with a higher initial director orientation angle. Furthermore, when the nematic orientation approaches the vertical configuration, i.e., when θ_0 is close to 90°, the onset of uniform thinning becomes more pronounced. The peak points on the solid curves indicate the completion of the Fréedericksz transition. It is also evident that for higher values of the initial orientation angle the LCE block undergoes a completed Fréedericksz transition at lower voltage levels.

The influence of the initial director orientation angle on the Fréedericksz transition can be examined from different perspectives through the relationship between the applied voltage difference and the stretch, as illustrated in Fig.7b. When the initial orientation angle is $\theta_0 = 5°$, a pronounced "S"-shaped response curve is clearly observed, indicating a strong manifestation of the Fréedericksz transition. However, as the initial angle increases to $\theta_0 \geq 30°$, the "S"-shaped behavior becomes less pronounced, suggesting that although the transition still occurs, its influence on the stretch response is significantly diminished. For very high values of the initial orientation angle, the transition has almost no observable effect on the stretch, and the characteristic "S"-shaped curve disappears entirely. It can be observed that achieving the same stretch value ($\lambda_1 > 1$) requires progressively higher voltages as the initial director angle θ_0 decreases. This behavior occurs because part of the supplied electrostatic energy is spent reorienting the mesogens toward

the direction of the electric field before macroscopic deformation can fully develop.

The following scenario illustrated in Fig.7c, displays the evolution of the director rotation angle θ for various values of the anisotropic step-length ratio r. It can be observed that an increased anisotropic ratio r necessitates a higher electric voltage to trigger the Fréedericksz transition, thereby increasing the threshold value. Furthermore, although larger values of r require greater voltage, the voltage range at which the Fréedericksz transition occurs remains nearly identical. Moreover, for values of ($r \geq 1.7$), an electric Fréedericksz transition is delayed, which implies less sensitivity to the electric field.

Further, Fig.7d illustrates the electric Fréedericksz transition in a voltage–stretch diagram for different values of r. When the initial orientation angle $\theta_0 = 5°$ is fixed and r is increased, the threshold voltage required to initiate the Fréedericksz transition increases significantly. The characteristic "S"-shaped response curves are closely associated with this transition: at low voltages, the nematic LCE block exhibits behavior similar to that of classical DE. As the applied voltage increases, the "S"-shaped response driven by mesogen reorientation, induces a sequence of mechanical deformations, including the longitudinal expansion, contraction, and subsequent re-expansion. This electro-mechanical behavior in LCEs is particularly valuable for designing soft actuators capable of two-side actuation.

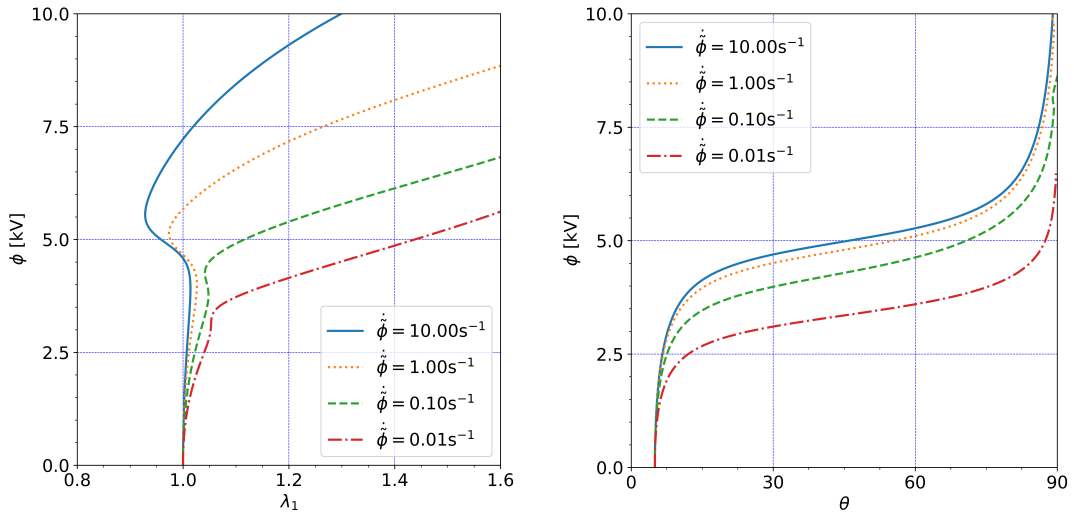

(a) (b)

Figure 8: Demonstration of the effect of different values of electric potential ramp rate $\dot{\phi} = 10.0, 1.0, 0.1,$ and 0.01 $[s^{-1}]$ on electric Fréedericksz transition phenomenon through: (a) Relationship between the applied voltage and the stretch λ_1; (b) Relationship between the applied voltage and the rotation angle of the director field θ. The length to thickness ratio is adopted as $L_x/L_y = 10$ while $r = 1.5$ and $\theta_0 = 5°$.

Fig.8 illustrates the influence of the ramp rate of the normalized electric potential on the evolution of deformation and the rotation of the director during the electric Fréedericksz transition. The relationship between the applied electric potential and the corresponding stretch for different ramp rates is shown in Fig.8a. It can be seen that a decrease in the electrical ramp rate leads to a reduction in the critical electric potential required to trigger the electric Fréedericksz transition. Consequently, the electric potential at which the LCE beam undergoes electrically induced thinning (i.e., contraction in the thickness direction) is also reduced, as the slower loading rate allows the viscoelastic stresses within the material to relax more effectively. On the other hand, when examining the evolution of the director orientation angle for different ramp rates, as shown in Fig.8b, a similar trend in the electric potential at which the electric Fréedericksz transition occurs can be observed. In particular, a plateau region emerges in which small variations in the electric potential lead to pronounced microstructural reorganization and progressive director rotation, resulting in its alignment with the direction of the electric field. Furthermore, as the electrical ramp rate decreases, viscoelastic effects become increasingly significant, leading to a softer material response and consequently reducing the electric potential required to induce director reorientation.

7.3. Bending actuation

Bending deformation in classical DEs is a well-understood phenomenon and represents a fundamental actuation mode in the design of soft actuators and robotic applications. In most configurations, such actuators consist of two layers with compliant electrodes: one electrode is attached to the top surface, while the second

electrode is embedded between the two layers of a cantilevered dielectric actuator. As the applied voltage increases from zero to a finite value, it is well established that the actuator bends to one side. This bending arises due to the Maxwell stress developed in the active dielectric layer where the electric field is present. In a similar configuration, two layers of nematic LCE dielectric are employed to form a cantilevered nematic LCE actuator. The resulting bending deformation is governed by the combined effects of the Fréedericksz transition, associated with director reorientation at lower electric voltages, and Maxwell stresses, which become dominant at higher voltage levels. This behavior reflects the complex electro-mechanical coupling inherent in nematic LCE materials.

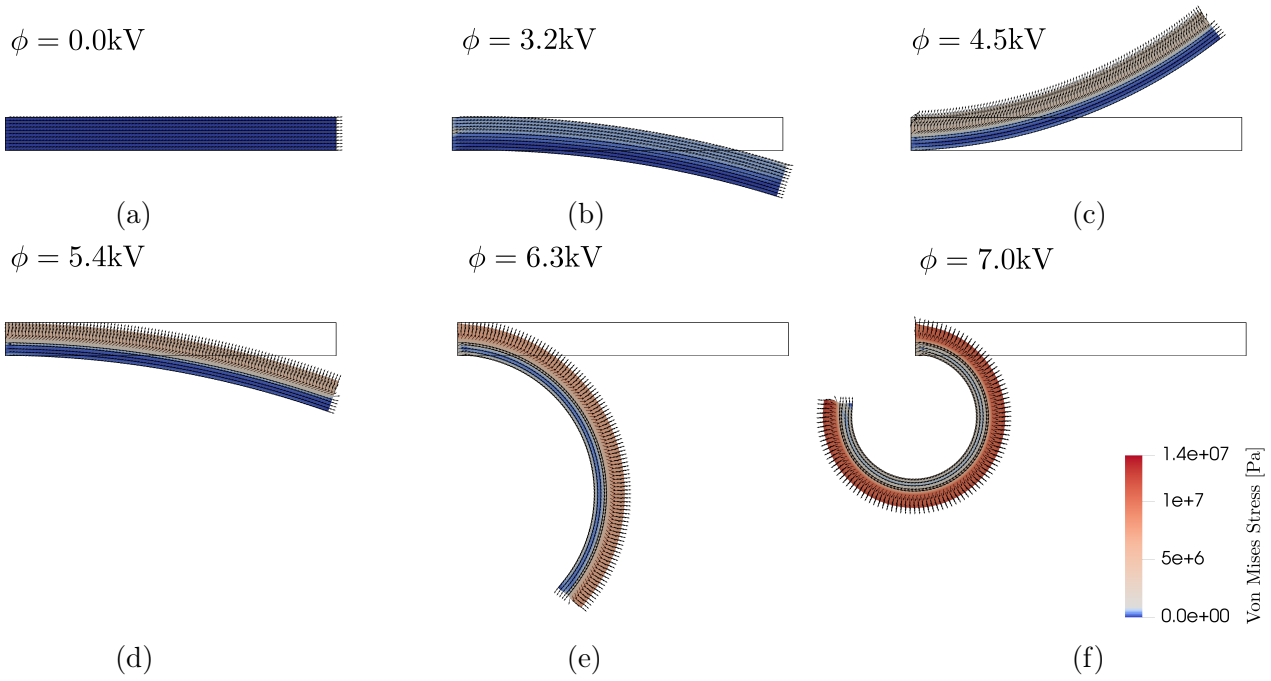

Figure 9: Snapshots from a quasi-static simulation showing the finite electro-viscoelastic two-sided electric bending actuation of a 2D nematic LCE solid-like beam and director field reorientation for incrementally applied voltage up to 7.0 kV, with electrical potential ramp rate $\dot{\phi} = 1.0$, and $r = 1.5$, $\theta_0 = 5^\circ$. (a) The nematic LCE sample with an initially distributed director field subjected to an electrostatic field at the initial increment corresponding to the zeroth applied voltage. (b) As the electrostatic field is applied, the Maxwell stresses induce cross-thickness compression and longitudinal extension of the electroactive upper layer, which leads to clockwise bending of the specimen. (c) With further increase in electric voltage, after the threshold value is exceeded, the director field begins to reorient and align with the electric field, resulting in cross-thickness extension and longitudinal compression of the upper layer, thus bending the LCE sample in counter-clockwise direction. (d)-(f) After the Fréedericksz transition is complete, further voltage increase leads to the dominance of Maxwell stress, causing the LCE beam to bend on the opposite side, forming a cylindrical shape. For this analysis, the length to thickness ratio is adopted as $L_x/L_y = 10$ and the middle compliant electrode is placed at $L_y/2$.

Fig.9 shows six snapshots of the finite-strain bending of a cantilever nematic LCE solid-beam under external electric actuation. In the first panel (Fig.9a), a finite nematic LCE actuator is shown, where the left edge is fixed, and both LCE layers possess identical nematic microstructures with the same initial orientation of director field. As the electric potential difference between the top and middle layer compliant electrodes increases, the actuator initially exhibits slight extension in the upper active layer that causes bending in the clockwise direction, as shown in Fig.9b. However, once the voltage reaches a critical value, a Fréedericksz transition occurs, leading to a reorientation of the nematic microstructure along the direction of the applied electric field. From a mechanical standpoint, this transition induces a contraction of the active layer in the lenght direction and bending of the cantilever LCE solid-beam in the counterclockwise direction (Fig.9c). After the completion of the Fréedericksz transition, a further increase in the applied voltage increases the Maxwell stress, which becomes the dominant force tending to induce compression in the thickness (extension in the length) direction of the upper layer of the nematic actuator. Finally, due to the difference in the overall stiffness between the electrically active and passive layers, the resulting deformation of the LCE actuator leads to bending in the clockwise direction, thereby forming a cylindrical shape (Fig.9d-f). Furthermore, it can be observed that while the initial orientation of the director in both layers is identical, during the Fréedericksz transition the nematic microstructure in the electrically actuated layer is almost entirely reoriented along

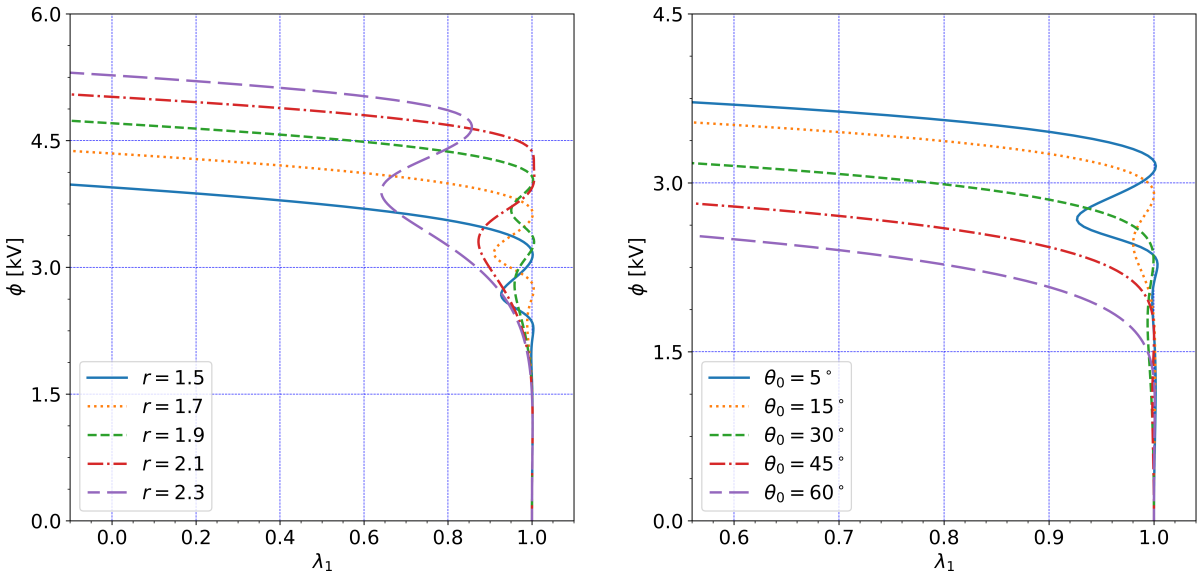

(a) (b)

Figure 10: Relationship between the applied voltage and the principal stretch λ_1, illustrating the finite bending deformation of the 2D LCE solid-beam for: (a) different values of the anisotropic step-length parameter ratio r; (b) different initial orientation angles θ_0 of the director field. The length to thickness ratio is adopted as $L_x/L_y = 10$, with electrical potential ramp rate $\dot{\tilde{\phi}} = 1.0$ and the middle compliant electrode placed at $L_y/2$.

the electric field. In contrast, the nematic microstructure in the electrically passive LCE layer tends to align with the direction of maximum stretch, which corresponds to the circular curvature that evolves during the deformation process.

Fig.10 shows the finite bending deformation of the LCE solid-beam subjected to an external electric field which is demonstrated through stretch-voltage response diagrams obtained for various values of the anisotropic step-length parameter ratio r and the initial orientation angle θ_0. In Fig.10a, the relationship between the applied voltage and the stretch λ_1 is shown for different values of the anisotropic step-length ratio in the range $r = 1.5$ to 2.3. It is evident that for lower values of r, the Fréedericksz transition develops and completes at lower voltages. As the anisotropic ratio increases, the system becomes less sensitive to the electric field, requiring higher voltages to initiate mesogen reorientation during large deformations of the LCE block. Furthermore, the initial orientation angle θ_0 significantly influences the large-deformation behavior of the LCE actuator, as illustrated in Fig.10b. For smaller values of θ_0, the response diagram exhibits a characteristic "S"-shaped curve, indicating a pronounced Fréedericksz transition. However, as θ_0 increases, the influence of this transition diminishes and becomes less noticeable in the stretch response. In the limiting case where $\theta_0 \to 60^\circ$, the LCE actuator exhibits fast director reorientation and one-side bending behavior similar to classical DE actuators.

Fig.11 illustrates the effect of the electric potential ramp rate on the electro-mechanical deformation of the LCE nematic actuator, highlighting both the Fréedericksz transition, which occurs at lower electric potentials, and the finite bending caused by the dominance of Maxwell stresses at higher voltage. To better understand the finite bending of viscoelastic LCE solid-beam, the evolution of the stretch (Fig.11a) and the corresponding director orientation (Fig.11b) are tracked. Note that the angle θ is measured from the positive direction of the x-axis and therefore, during bending, the measured director orientation angle may exceed 90°. As can be observed from Fig.11a, an increase of the electric ramp rates delays the initiation of the Fréedericksz transition, since the system becomes stiffer and its elastic properties dominate. Moreover, once the Fréedericksz transition is completed and the electric potential continues to increase, the deformation rises monotonically due to the dominance of Maxwell's stresses. An additional interesting phenomenon occurs at slower ramp rates: the Fréedericksz transition is completed more rapidly compared to higher rates, resulting in noticeably smaller deformations during actuation. This effect is even more pronounced in Fig.11b, where the evolution of the director orientation angle is tracked. For higher ramp rates, the response curves show a flat region during the Fréedericksz transition, after which the directors gradually realign according to the electro-mechanical response. In general, faster electrical ramp rates result in a stiffer response, where the system behaves in a nearly elastic manner. Conversely, when the rates are slower, the material response

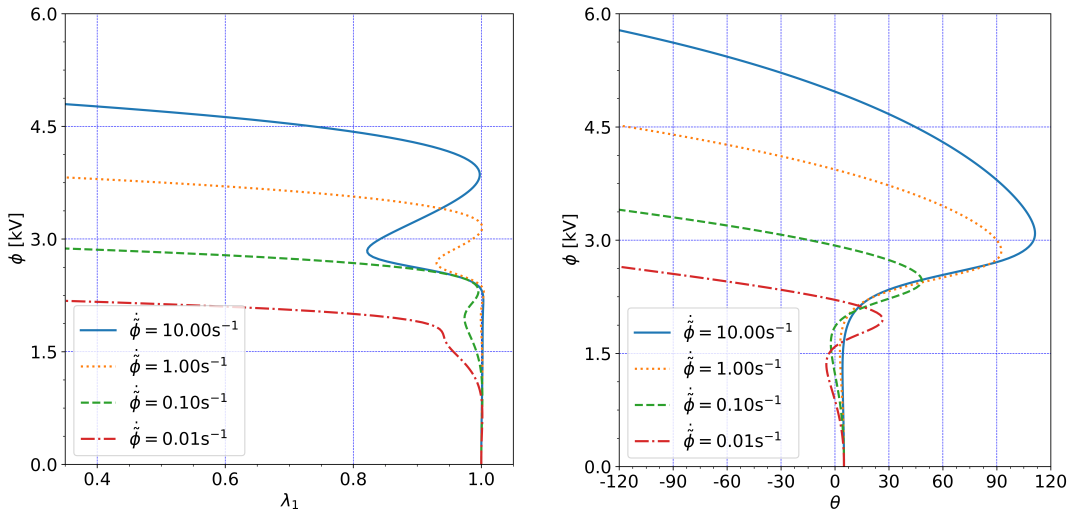

(a) (b)

Figure 11: Demonstration of the effect of different electric potential ramp rates on electro-mechanical bending of the 2D LCE block through: (a) Relationship between the applied voltage and the stretch λ_1; (b) Relationship between the applied voltage and the rotation angle of the director field θ. The simulations are performed for different values of electric potential ramp rates $\dot{\tilde{\phi}} = 10.0, 1.0, 0.1,$ and $0.01\ s^{-1}$ when $r = 1.5$ and $\theta_0 = 5°$. The length to thickness ratio is $L_x/L_y = 10$ and the middle compliant electrode is placed at $L_y/2$. The angle θ is measured from the positive direction of the x-axis.

becomes softer, exhibiting relaxation effects that are more physically realistic for LCE materials. In the design of soft actuators, the rate of applying deformation or electric loading represents a fundamental condition to ensure the proper functionality of such systems.

7.4. Buckling instability

The following numerical examples investigate the electro-mechanical buckling of an LCE actuator composed of two layers with identical nematic microstructures, which together form a solid-beam structure. In contrast to the previously analyzed cantilever actuator, the present configuration considers a two-dimensional LCE block with both the left and right edges fixed. This setup imposes constraints on displacements in both the axial and transverse directions, thereby fundamentally altering the nature of the electro-mechanical response.

Fig.12 shows six sequential snapshots illustrating the evolution of electro-mechanical instability in the form of in-plane buckling. The instability is preceded by a Fréedericksz transition at lower voltage levels, after which the dominance of Maxwell stresses at higher voltages induces the electro-mechanical instability. In the first panel (Fig.12a), the undeformed configuration of the bi-layer LCE actuator is shown. One compliant electrode is attached to the top surface, while the other is embedded at the mid-plane. As the voltage increases from zero to a critical value, the nematic directors in the actuated layer begin to rotate (Fig.12b). Upon completion of the Fréedericksz transition, the directors become nearly aligned with the electric field direction, as shown in Fig.12c. A further increase in the electric potential causes the Maxwell stress to dominate as the main driving force, leading to the development of in-plane compressive stresses within the actuated layer, which would result in significant deformation. Owing to the fully constrained boundary conditions that suppress in-plane extension, the system becomes unstable, leading to in-plane buckling of the LCE solid-beam (Fig.12d–f). This example demonstrates the critical influence of boundary conditions on the transition from smooth actuation (as observed in the fixed-free case) to electro-mechanical instability in constrained geometries.

In the present study, the threshold voltage is defined as the critical value of the applied electric potential at which the soft nematic dielectric exhibits the onset of buckling instability. Below this threshold, the material remains close to its initial configuration, whereas exceeding it leads to the emergence of large electro-mechanically induced deformations and the subsequent growth of instability.

Fig.13 illustrates the threshold voltage values associated with the onset of electro-mechanical buckling in the LCE actuator. Panel (a) highlights the influence of the anisotropic step-length ratio r, while panel (b) demonstrates the effect of the initial director orientation angle θ_0 on the emergence of bulk instability. In general, the threshold voltage corresponds to the abrupt change in the vertical segment of the voltage–stretch

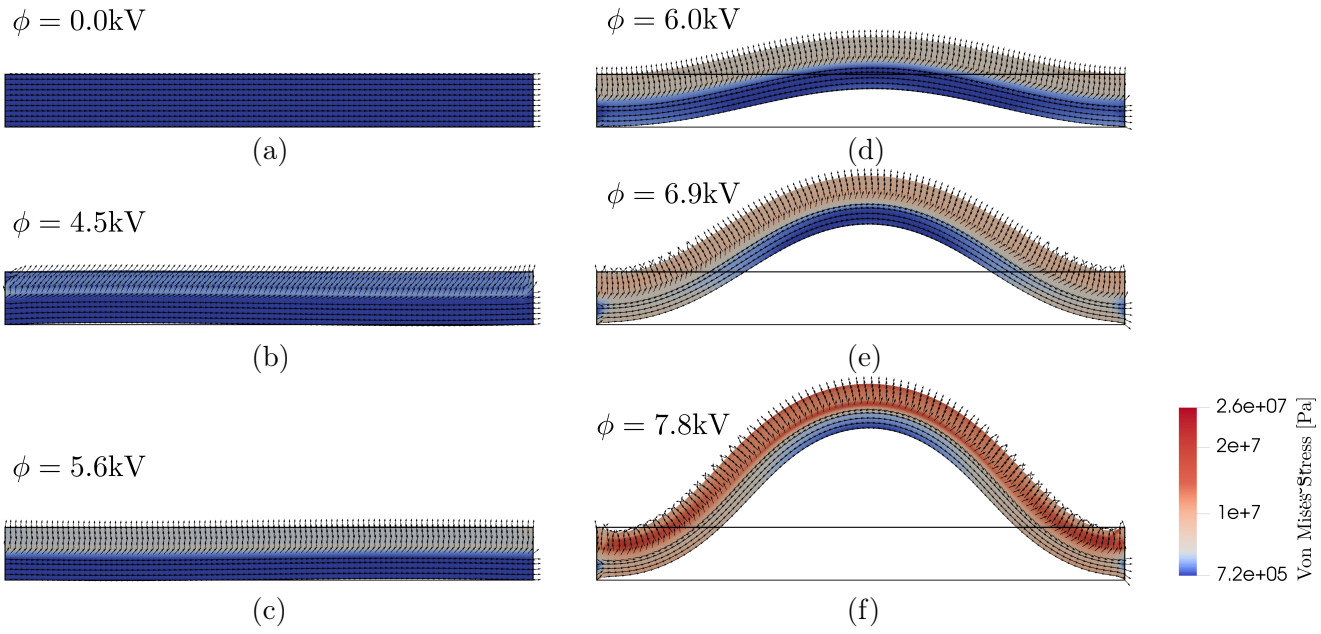

Figure 12: Snapshots from a quasi-static simulation illustrating electro-viscoelastic buckling in a bi-layer LCE sample with electrodes placed on the top and in the middle plane. The simulation demonstrates orientation of the director field under an incrementally applied voltage up to 7.8 kV, with the electrical potential ramp rate $\dot{\tilde{\phi}} = 1.0$, $r = 1.5$ and $\theta_0 = 5°$. (a) The nematic LCE sample, with an initially distributed director field, is subjected to an electrostatic field at the initial (zeroth) increment, corresponding to zero applied voltage. (b)-(c) As the electric field increases, the director field begins to reorient. (d) The directors align with the electric field, causing expansion in the upper layer due to dominant Maxwell stresses and initiating buckling. (e)-(f) The bi-layer sample exhibits pronounced buckling under the maximum applied electric field. The length to thickness ratio is adopted as $L_x/L_y = 10$ and the middle compliant electrode is placed at $L_y/2$.

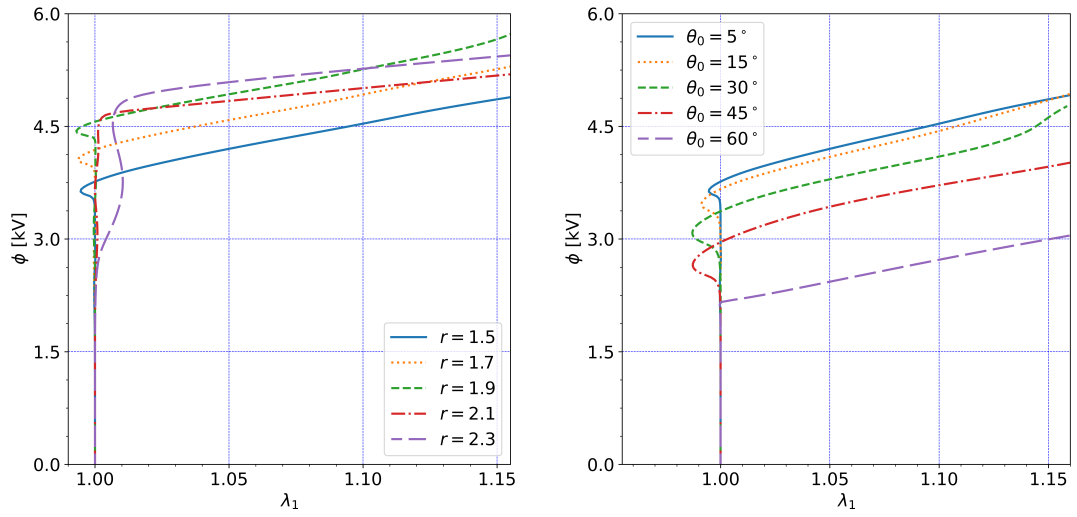

Figure 13: Relationship between the applied voltage and the principal stretch λ_1, illustrating the onset of electro-mechanical buckling in the 2D LCE block for: (a) different values of the anisotropic step-length parameter ratio r; (b) different initial orientation angles of the director field θ_0. The length to thickness ratio is adopted as $L_x/L_y = 10$ and electrical potential ramp rate $\dot{\tilde{\phi}} = 1.0$, with the middle compliant electrode placed at $L_y/2$..

response curve, clearly observable in both subfigures as a marker of critical value of voltage for electro-mechanical buckling. Prior to reaching this critical point, the system undergoes a Fréedericksz transition, which manifests as a modest perturbation in the stretch response due to the gradual reorientation of mesogens. However, once the applied voltage exceeds the critical value, a pronounced and rapid increase in stretch occurs, indicating the onset of large-scale deformation driven by electro-mechanical buckling instability. From Fig.13a, it can be observed that increasing the anisotropic step-length ratio r, leads to a noticeable rise

in the critical buckling voltage. From the physical point of view, a higher value of r implies greater anisotropy along the preferred director, enhancing the stiffness of the system in the direction of actuation. Consequently, a stronger electric field is required to trigger electro-mechanical instability. Conversely, Fig.13b shows that the initial orientation angle θ_0 of the director field also significantly influences the critical voltage, but in an opposite manner. At higher values of θ_0, the Fréedericksz transition occurs rapidly with minimal deformation, reducing the energy required to trigger instability and thus lowering the critical buckling voltage. Moreover, for lower values of θ_0, the Fréedericksz transition which appears prior to buckling is more pronounced in the response curves. In such cases, the threshold voltage is comparatively higher, as the system requires substantial mesogen reorientation and associated deformation before electro-mechanical buckling initiates.

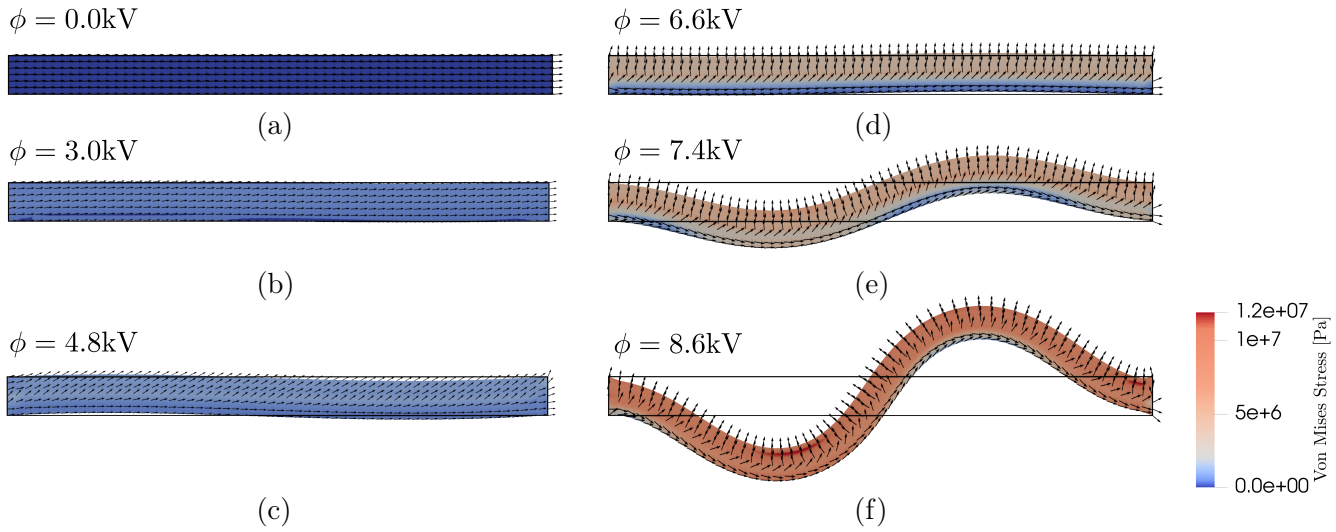

Figure 14: Snapshots from a quasi-static simulation showing finite electro-viscoelastic buckling of a bi-layer 2D LCE solid-beam in the second buckling mode. The simulation captures director field reorientation under an incrementally applied voltage up to 8.6 kV, and adopted anisotropic step-length ratio $r = 1.5$, electrical potential ramp rate $\dot{\phi} = 1.0$, the length-to-thickness ratio $L_x/L_y = 14$ and the middle compliant electrode placed at $L_y/3$. (a) The nematic LCE sample, with an initially distributed director field, is subjected to an electrostatic field at the zeroth increment, corresponding to zero applied voltage. (b) Once the Fréedericksz transition threshold value is reached, the director field begins to rotate. (c) As the electric field increases, the director field begins to reorient. (d) The directors align with the electric field, leading to the onset of the second buckling mode. (e)-(f) The 2D bi-layer sample exhibits pronounced buckling under the maximum applied electric field.

Fig.14 presents six sequential snapshots illustrating the evolution of electro-mechanical instability in the form of in-plane buckling. The sequence captures the progressive development of deformation as the applied electric potential increases, revealing the transition from the nearly undeformed configuration to a well-developed pattern corresponding to the second mode. The two-dimensional sample consists of two compliant electrodes, one positioned on the top surface and the other embedded between the two LCE layers at $L_y/3$. For this analysis, a sample with a length-to-width ratio of $L_x/L_y = 14$ is considered. In the first panel, Fig.14a, the undeformed configuration of the bi-layer LCE solid beam is shown. As the applied voltage increases, it reaches the critical threshold (Fig.14b), beyond which further voltage induces rotation of the nematic directors in the electrically actuated layer (Fig.14c). Upon completion of this Fréedericksz transition, the directors become nearly aligned with the electric field, as depicted in Fig.14d. The resulting mesogen rotation introduces a localized perturbation in the specimen's shape, which, under additional voltage, amplifies the Maxwell stresses and triggers the onset of electro-mechanical instability. Consequently, the beam deforms into a well-defined second buckling mode, as illustrated in Fig.14e and f. This sequence highlights the intricate interplay between director reorientation, electrostatic loading, and viscoelastic response in shaping the progressive development of the buckled configuration.

The influence of the electric ramp rate on the electro-mechanical buckling of the bi-layer LCE nematic actuator is illustrated in Fig.15 and Fig.16. The system's response is characterized through the stretch–voltage and director orientation–voltage relations, with results presented for a range of applied ramp rates. These plots reveal how variations in the rate of voltage application affect both the onset of instability and the progressive rotation of the nematic directors, highlighting the interplay between viscoelastic relaxation and electro-mechanical coupling in shaping the actuator's deformation behavior.

Fig.15 illustrates a case in which the LCE solid beam has a length-to-thickness ratio of $L_x/L_y = 10$,

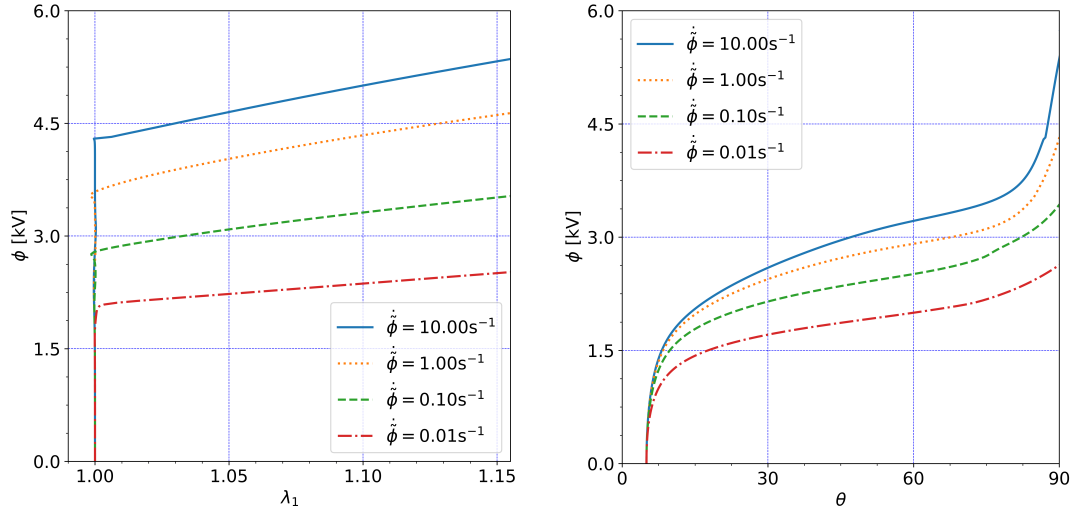

(a) (b)

Figure 15: Demonstration of the effects electric potential ramp rates on electro-mechanical buckling of the LCE solid-beam through: (a) Relationship between the applied voltage and the stretch λ_1; (b) Relationship between the applied voltage and the rotation angle of the director field θ. The simulations are performed for different values of electric potential ramp rates $\dot{\tilde{\phi}} = 10.0, 1.0, 0.1,$ and $0.01\ s^{-1}$ when $r = 1.5$ and $\theta_0 = 5°$. The length to thickness ratio is adopted as $L_x/L_y = 10$ and the middle compliant electrode is placed at $L_y/2$.

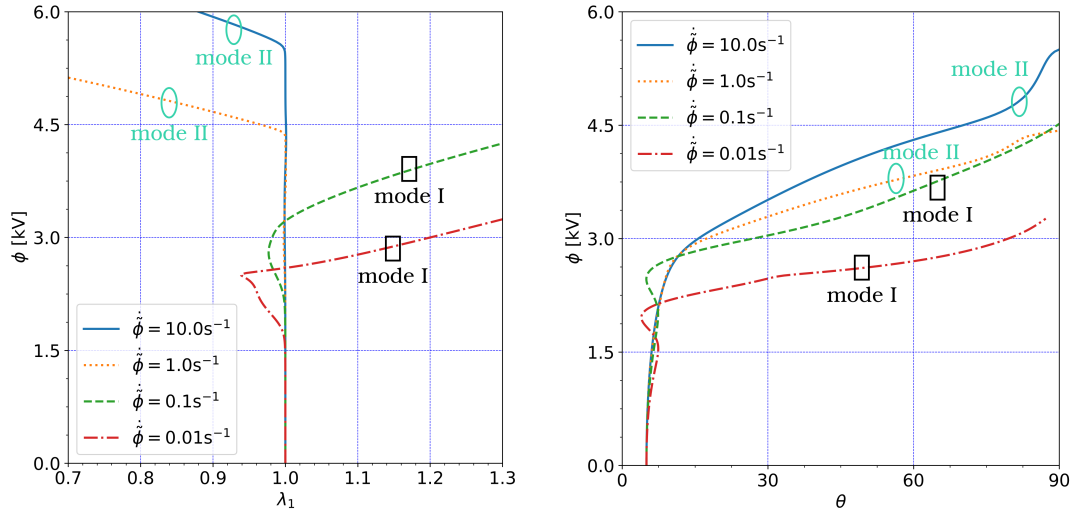

(a) (b)

Figure 16: Demonstration of the effects electric potential ramp rates on electro-mechanical buckling of the LCE's solid-like beam through: (a) Relationship between the applied voltage and the stretch λ_1 ; (b) Relationship between the applied voltage and the rotation angle of the director field θ. The simulations are performed for different values of electric potential ramp rates $\dot{\tilde{\phi}} = 10.0, 1.0, 0.1,$ and $0.01\ s^{-1}$ when $r = 1.5$ and $\theta_0 = 5°$. The length to thickness ratio is adopted as $L_x/L_y = 14$ and the middle compliant electrode is placed at $L_y/3$. The angle θ is measured from the positive direction of the x-axis

with the lower electrode positioned at $L_y/2$. In contrast, Fig.16 depicts a system with $L_x/L_y = 14$, where the lower electrode is located at $L_y/3$. In both configurations, the upper electrode is attached to the top surface of the LCE beam, providing a consistent electrical boundary condition. From a physical standpoint, it is particularly noteworthy that the buckling mode is strongly governed by the rate at which the electric potential is applied. Specifically, as it can be seen from Fig.16, for higher ramp rates, the actuator undergoes electro-mechanical buckling in the second mode, whereas for lower ramp rates, the first buckling mode arises as a consequence of the intrinsic viscoelastic material properties. However, this observation should not be regarded as a general conclusion, since the instability of system exhibits strong sensitivity to both material and geometric parameters, necessitating a case-by-case investigation. From a physical perspective, it can be concluded that higher ramp rates correspond to a predominantly elastic response, characterized by a markedly stiffer mode, in which the nonequilibrium contribution has insufficient time to relax and the

system reacts almost instantaneously. In contrast, at slower ramp rates, the system exhibits more pronounced viscoelastic properties, allowing the nonequilibrium component greater time to relax, thereby shaping the overall electro-mechanical response emerge at lower energy mode.

Panel (a) of Fig.15 and Fig.16 illustrates the threshold corresponding to the critical electric potential at which electro-mechanical buckling is initiated. Prior to reaching this threshold, the deformation remains essentially unperturbed during Fréedericksz transition, highlighting the sudden onset of instability once the critical condition is surpassed. When the electric potential reaches this critical value, even a small variation in increasing electric potential produces significant changes in the deformation response. Moreover, decreasing the electric ramp rates leads to a reduction in the critical electric potential required for the onset of electro-mechanical buckling. However, by tracking the change in the director orientation angle during the variation of the voltage, a smooth transition of the director is observed for all ramp rates that are presented in panels (b) of Fig.15 and Fig.16. Furthermore, the evolution of the director orientation allows the identification of the buckling mode. For a point selected in the middle of the electrically actuated layer, for the first buckling mode the director at that point reaches a vertical position. In the second mode, the director at the selected point continues to rotate until the nematic actuator reaches its final configuration, and the orientation angle can exceed $\pi/2$. In general, for an accurate determination of the buckling mode, it is recommended to visualize each mode for all loading electric ramp rates, as these factors can significantly affect the initiation and development of electro-mechanical instabilities.

This rate-dependent transition between buckling modes can be further explored by comparing the instability mechanisms in conventional DEs with those in LCEs. In classical DEs electro-mechanical buckling emerges after material expansion solely due to Maxwell stresses. In LCEs, the buckling mechanism is notably more complex due to coupled effects of stresses induced by mesogen rotation through the electric Fréedericksz transition and electrostatic Maxwell stresses. The mesogen rotation in LCEs introduces an additional viscoelastic mechanisms absent in conventional DEs. This could explain why the buckling mode itself becomes rate-dependent: at high ramp rates, the material responds in a stiff manner, favoring higher-order buckling modes; at low rates, viscoelastic relaxation and progressive director rotation soften the material, allowing the system to attain the lower-energy first mode. While both DEs and LCEs exhibit rate-dependent buckling due to viscoelasticity, LCEs present a more complex buckling behavior that is governed by the interplay between the mechanical relaxation and nematic microstructural effects. However, in order to confirm the physical realizability of the predicted buckling modes, it is essential to perform experimental validation under comparable conditions, particularly with respect to specimen geometry and the ramp rates investigated herein.

The viscoelastic rate-dependent behavior of LCEs is qualitatively similar to the one observed in conventional DEs (e.g. see [69]), but with a key distinction arising from the material's internal structure. In DEs, decreasing the loading rate allows sufficient time for the relaxation of viscoelastic mechanisms, resulting in a softer material response and consequently a lower critical electric potential for the onset of instability. In the limit of an infinitely slow ramp rate, these mechanisms are always fully relaxed, and the critical electric potential approaches the equilibrium value. In the present LCE system, however, this rate-dependent softening is additionally influenced by the coupling between viscoelastic relaxation and the progressive reorientation of LC mesogens. Thus, while both material classes exhibit a delayed instability at higher rates due to the increased effective stiffness, LCEs display an additional reduction in the critical electric potential, attributed to the combined effect of mechanical relaxation and mesogen realignment along the electric field.

8. Conclusions

A theoretical modeling framework with numerical implementation of an electro-visco-hyperelastic nematic LCE presented in this study constitutes a significant contribution to the systematic modeling of electro-mechanical phenomena, particularly the Fréedericksz transition, finite deformation and buckling. While this phenomenon is well-documented in the LC literature, existing models for LCEs have been largely limited to the elastic-deformation regime. In contrast, the current work generalizes the description to the viscoelastic finite-deformation regime, deriving a complete set of governing equations within the framework of continuum thermodynamics. By applying the principle of virtual power, the governing balance laws for linear and angular momentum, as well as balance law for the director field, have been systematically derived. Assuming an isothermal process and an additive decomposition of the Helmholtz free energy along with the Flory and Sidoroff decomposition of the deformation gradient, the Coleman–Noll procedure was employed to obtain the corresponding constitutive relations. Furthermore, the adopted form of the free energy accounts for

the semi-soft elasticity characteristic of LCE, which fundamentally arises from the rotation of mesogen units. The complete formulation has been specialized to the plane strain setting and prepared for numerical implementation using the open-source finite element platform FEniCSx. An additional contribution of this study lies in the exploration of Fréedericksz transition-driven electro-mechanical deformations for the design of advanced micro-electro-mechanical devices, including the two-side bending actuators, artificial muscles and soft robotic applications. Furthermore, the electro-viscoelastic phenomena observed in nematic LCEs may serve as a foundational framework for the development of active metamaterials, sensing devices and waveguides.

A key finding is the identification of a new class of instability that combines the Fréedericksz transition and Maxwell stresses to produce electro-mechanical buckling in a solid-beam configuration under electric loading. In conventional DE with in-plane constraints, electrically induced buckling typically emerges as a bifurcation after the material expands due to Maxwell stresses. In LCEs, however, an additional mechanism of the mesogen rotation is present, which strongly influences both the onset and the shape of the buckling instability. Furthermore, we observed rate-dependence of buckling modes in LCEs highlighting the strong coupling between microstructural evolution and electro-mechanical instability. Notably, no geometric imperfections are required, as the inhomogeneous mesogen rotation inherently induces spatial stiffness variations that trigger instability. Such effects may be utilized for voltage-controlled active switches and actuators operating near the critical thresholds. Overall, the presented results reveal two distinct rate-dependent regimes: at faster ramp rates, viscoelastic effects associated with non-equilibrium mechanisms do not have sufficient time to relax, so the material response approaches that of a purely elastic solid, leading to more constrained electro-mechanical behavior. However, at slower ramp rates of the applied electric potential, the non-equilibrium mechanisms have enough time to relax, resulting in a softer overall response and lower electric potentials required to trigger electro-mechanical deformation and buckling.

Future research directions may include: (a) exploring electro-wrinkling, electro-creasing, electro-mechanical cavitation, and electro-elastic capillarity phenomena, which remain largely unexplored in nematic LCEs but offer promising avenues for new actuation and morphing capabilities; (b) investigating flexoelectric coupling, particularly relevant at small scales, which can significantly affect electro-mechanical responses and enable novel MEMS and soft energy-harvesting devices; (c) exploring the influence of temperature; and (d) performing complementary experiments to validate and further refine the theoretical predictions presented here.

Credit authorship contribution statement

Danilo Karličić: Conceptualization, Methodology, Computations, Writing – original draft, Writing – review & editing. **Milan Cajić**: Computations, Software, Writing – original draft, Writing – review & editing. **Stepa Paunović**: Computations, Software, Writing – review & editing. **Mokarram Hossain**: Writing – original draft, Methodology, Writing – review & editing, Supervision.

Declaration of competing interest

The authors declare that they have no known competing financial interests or personal relationships that could have appeared to influence the work reported in this paper.

Data availability

Data will be made available on request.

Acknowledgements

The authors acknowledge the support of the Serbian Ministry of Science, Technological Development and Innovation through the Mathematical Institute of the Serbian Academy of Sciences and Arts.

Appendix A. The second requirement of the virtual power principle

Starting from the second requirement of the virtual power principle $\mathcal{W}^{+}_{int}(\mathcal{P},\mathcal{V}^{+}) = \mathcal{W}_{int}(\mathcal{P},\mathcal{V})$ or the frame indifference of the internal power, the generalized set of the virtual velocities in the new frame is defined as

$$\mathcal{V}^{+} = (\tilde{\boldsymbol{\chi}}^{+}, \tilde{\mathbf{F}}^{+}, \tilde{\mathbf{n}}^{+}, \tilde{\mathbf{H}}^{+}, \tilde{\phi}^{+}). \tag{A.1}$$

Further, we define scalar, vector and tensor fields in the new frame as

$$\boldsymbol{\chi}^{+} = \mathbf{Q}\boldsymbol{\chi} + \mathbf{c}, \quad \tilde{\phi}^{+} = \tilde{\phi}, \quad \mathbf{n}^{+} = \mathbf{Q}\mathbf{n}, \quad \mathbf{Q}\mathbf{Q}^{T} = \mathbf{I}, \tag{A.2}$$

$$\tilde{\boldsymbol{\chi}}^{+} = \dot{\mathbf{Q}}\boldsymbol{\chi} + \mathbf{Q}\tilde{\boldsymbol{\chi}} + \tilde{\mathbf{c}}, \quad \tilde{\mathbf{n}}^{+} = \dot{\mathbf{Q}}\mathbf{n} + \mathbf{Q}\tilde{\mathbf{n}},$$

and

$$\mathbf{F}^{+} = \mathbf{Q}\mathbf{F}, \quad \mathbf{H}^{+} = \mathbf{Q}\mathbf{H}, \tag{A.3}$$

$$\tilde{\mathbf{F}}^{+} = \dot{\mathbf{Q}}\mathbf{F} + \mathbf{Q}\tilde{\mathbf{F}}, \quad \tilde{\mathbf{H}}^{+} = \dot{\mathbf{Q}}\mathbf{H} + \mathbf{Q}\tilde{\mathbf{H}},$$

where $\mathbf{Q}$ is the proper orthogonal tensor with $\det\mathbf{Q} = 1$, and vectors defined in the reference configuration stay unchanged $\mathbf{d}^{+}_{R} = \mathbf{d}_{R}$ and $\mathbf{e}^{+}_{R} = \mathbf{e}_{R}$.

The change of internal virtual power $\mathcal{W}^{+}_{int}(\mathcal{P},\mathcal{V}^{+})$, under the new frame can be expressed as:

$$\mathcal{W}^{+}_{int}(\mathcal{P},\mathcal{V}^{+}) = \int_{\mathcal{P}} \left(\mathbf{P}^{+}_{\mathrm{T}} : \tilde{\mathbf{F}}^{+} + \boldsymbol{\Sigma}^{+} : \tilde{\mathbf{H}}^{+} - \boldsymbol{\pi}^{+} \cdot \tilde{\mathbf{n}}^{+} + \mathbf{d}^{+}_{R} \cdot \tilde{\mathbf{e}}^{+}_{R} \right) dv_{R}. \tag{A.4}$$

Introducing Eq.(A.2) and Eq.(A.3) into Eq.(A.4), and equating the result with Eq.(19), yields

$$\int_{\mathcal{P}} \left[\dot{\mathbf{Q}} : \left(-\boldsymbol{\pi}^{+} \otimes \mathbf{n} + \mathbf{P}^{+}_{\mathrm{T}}\mathbf{F}^{T} + \boldsymbol{\Sigma}^{+}\mathbf{H}^{T} \right) \right] dv_{R} = 0. \tag{A.5}$$

This results in the following transformed fields

$$\boldsymbol{\pi}^{+} = \mathbf{Q}\boldsymbol{\pi}, \quad \mathbf{P}^{+}_{\mathrm{T}} = \mathbf{Q}\mathbf{P}_{\mathrm{T}}, \quad \boldsymbol{\Sigma}^{+} = \mathbf{Q}\boldsymbol{\Sigma}, \tag{A.6}$$

where $\boldsymbol{\pi}$ is the vector filed, while $\mathbf{P}_{\mathrm{T}}$ and $\boldsymbol{\Sigma}$ are two point tensor fields. Assuming that the $\mathbf{Q}^{T}\dot{\mathbf{Q}} = -(\mathbf{Q}^{T}\dot{\mathbf{Q}})^{T}$ is the skew-symmetric tensor, we obtain the coupled balance law for angular momentum as

$$\mathrm{skw}\left(-\boldsymbol{\pi} \otimes \mathbf{n} + \mathbf{P}_{\mathrm{T}}\mathbf{F}^{T} + \boldsymbol{\Sigma}\mathbf{H}^{T} \right) = \mathbf{0}, \tag{A.7}$$

where we can recognize the Kirchhoff stress tensor $\boldsymbol{\tau}_{\mathrm{T}} = \mathbf{P}_{\mathrm{T}}\mathbf{F}^{T}$.

Finally, the balance laws take the following form:

$$\mathrm{Div}\mathbf{P}_{\mathrm{T}} + \mathbf{b}_{R} = \rho_{R}\mathbf{a}, \tag{A.8}$$

$$\mathrm{Div}\boldsymbol{\Sigma} + \boldsymbol{\pi} = \mathbf{0}, \tag{A.9}$$

$$\mathrm{skw}\boldsymbol{\tau}_{\mathrm{T}} = -\mathrm{skw}\left(-\boldsymbol{\pi} \otimes \mathbf{n} + \boldsymbol{\Sigma}\mathbf{H}^{T} \right), \tag{A.10}$$

under the assumption of macroscopic inertial effects, where the body force is modified as

$$\mathbf{b}_{R} \to \mathbf{b}_{R} - \rho_{R}\mathbf{a},$$

and excluding microscopic body forces or external orientational body forces related to internal body couples $\boldsymbol{\gamma}$.

Appendix B. Electrostatics

In the general electrostatic case, two Maxwell's equations must be satisfied for polarized media, namely Faraday's law and Gauss's law [50, 69, 73]:

$$\text{curl}\mathbf{e} = \mathbf{0} \quad \text{and} \quad \text{div}\mathbf{d} = 0, \tag{B.1}$$

which are presented here in their spatial (Eulerian) form, as commonly stated in physics. In this context, we assume that the free charge density is negligible. The vector field $\mathbf{e}$ represents the electric field, which satisfies Faraday's law and can be expressed as $\mathbf{e} = -\nabla\phi$, where ϕ is the scalar electric potential. The second equation corresponds to Gauss's law, where $\mathbf{d}$ denotes the electric displacement field.

By assuming that the nematic LCE exhibits anisotropic electric properties, the general electric constitutive equation for polarized media remains valid:

$$\mathbf{d} = \epsilon_0\mathbf{e} + \mathbf{p}, \tag{B.2}$$

where $\mathbf{p}$ denotes the polarization vector. For materials with electrical anisotropy, such as nematic LCEs, the polarization is no longer simply proportional to the electric field via a scalar electric susceptibility. Instead, the polarization is governed by a second-order electric susceptibility tensor, reflecting the directional dependence of the material's polarizability. This anisotropic behavior arises from the internal alignment of mesogens within the polymer network, which induces preferential polarization directions [23, 50].

In what follows, we focus on the parametrization of the material's electric response through the electric field $\mathbf{e}$ and the electric displacement field $\mathbf{d}$. The relationship between these two fields depends on the director field $\mathbf{n}$, leading to the dielectric permittivity tensor [50]:

$$\mathbb{D}_n = (\epsilon_c - \epsilon_a)\mathbf{n}\otimes\mathbf{n} + \epsilon_a\mathbf{I}, \tag{B.3}$$

where $\epsilon_a = \epsilon_0\epsilon_\perp$ and $\epsilon_c = \epsilon_0\epsilon_\parallel$ are the electric permittivities perpendicular and parallel to the director field $\mathbf{n}$, respectively, and $\epsilon_0 = 8.85\times10^{-12}\,\text{F/m}$ is the vacuum permittivity. We also define the dielectric anisotropy ratio as $r_\epsilon = \epsilon_\parallel/\epsilon_\perp$. The corresponding electric constitutive relation in the current configuration is given by:

$$\mathbf{d} = \mathbb{D}_n\mathbf{e}. \tag{B.4}$$

In general, for applications in solid mechanics, a more convenient form of Maxwell's equations is their expression in the reference configuration [74, 75],

$$\text{Curl}\mathbf{e}_R = \mathbf{0} \quad \text{and} \quad \text{Div}\mathbf{d}_R = 0, \tag{B.5}$$

leading to referential form of electric field vector $\mathbf{e}_R$ and electric displacement $\mathbf{d}_R$, derived as

$$\mathbf{e}_R = -\nabla\phi = \mathbf{F}^T\mathbf{e} \quad \text{and} \quad \mathbf{d}_R = \text{J}\mathbf{F}^{-1}\mathbf{d}, \tag{B.6}$$

The electric constitutive relation between $\mathbf{d}_R$ and $\mathbf{e}_R$ is determined as

$$\mathbf{d}_R = \text{J}\mathbf{F}^{-1}\mathbb{D}_n\mathbf{F}^{-T}\mathbf{e}_R. \tag{B.7}$$

Appendix C. Constitutive relations

Appendix C.1. Stress tensors

Before proceeding with the derivation of the specific stress tensors characterizing the multi-branch Maxwell model for a viscoelastic material, where the multiplicative decomposition of the deformation gradient is employed, $\mathbf{F} = \mathbf{F}^{e(i)}\mathbf{F}^{v(i)}$, $(i = 0, 1, ..., N)$, we first need to define the following branches according to [55]:

- The equilibrium branch, corresponding to the elastic response of the material, is denoted by $i = 0$ and

$$\mathbf{F}^{e(i=0)} = \mathbf{F} \quad \text{and} \quad \mathbf{F}^{v(i=0)} = \mathbf{I}. \tag{C.1}$$

- The non-equilibrium branches related to the viscoelastic response of the material are denoted as $i = 1, .., M$.

- The viscous distortion is isochoric, $\det\mathbf{F}^{v(i)} = 1$, leading to the conditions, $\mathrm{J} = \mathrm{J}^{e(i)}$ for all i.

From the second terms in Eq.(39), Eq.(48), and Eq.(C.1), we can additively decompose the Kirchhoff stress tensor as

$$\boldsymbol{\tau} = \sum_{i=0}^{M} \boldsymbol{\tau}^{(i)} = \boldsymbol{\tau}^{(0)} + \sum_{i=1}^{M} \boldsymbol{\tau}^{(i)NEQ} = \left(\mathbf{P}^{(0)} + \sum_{i=1}^{M} \mathbf{P}^{e(i)NEQ} \right) \mathbf{F}^{T} = \mathbf{P}\mathbf{F}^{T}, \tag{C.2}$$

and correspondingly the first Piola–Kirchhoff stress tensor as

$$\boxed{\mathbf{P} = \mathbf{P}^{(0)} + \sum_{i=1}^{M} \mathbf{P}^{e(i)NEQ} = \mathbf{P}^{EQ} + \mathbf{P}^{anis} + \mathbf{P}^{Frank} + \mathbf{P}^{MW} + \mathbf{P}^{NEQ},} \tag{C.3}$$

where $\mathbf{P}^{(0)}$ is determined from Eq.(48) as

$$\mathbf{P}^{(0)} = \frac{\partial \psi_R^{(0)}}{\partial \mathbf{F}}, \tag{C.4}$$

in which

$$\psi_R^{(0)} = \psi_R^{EQ} + \psi_R^{anis} + \psi_R^{Vol} + \psi_R^{Frank} + \psi_R^{Elec}. \tag{C.5}$$

In the following, we set out all the stress tensors corresponding to the presented electro-viscohyperelastic model of the dielectric LCE with nematic microstructures.

Non-equilibrium stress tensors

Applying the Eq.(59) into Eq.(48) and using Eq.(9) and Eq.(10), we can determine the elastic first Piola-Kirchhoff stress tensor for the $i-th$ non-equilibrium branch as

$$\mathbf{P}^{e(i)NEQ} = \mu_{(i)}^{NEQ} \left[\overline{g}_0^{e(i)} \overline{\mathbf{K}}_0^{e(i)} - \left(\frac{m}{a_0} \right) \|\overline{\mathbf{n}}_{\overline{\mathbf{F}}^{e(i)}}\|^2 \overline{a}_{t(i)}^2 \overline{\mathbf{B}}_0^{e(i)} + \overline{a}_{(i)} \overline{\mathbf{Z}}_0^{e(i)} \right] \mathbf{F}^{-T}, \tag{C.6}$$

in which deviatoric parts of the following isochoric tensors are defined as

$$\overline{\mathbf{K}}_0^{e(i)} = \mathbb{A} : \overline{\mathbf{K}}^{e(i)}, \quad \overline{\mathbf{B}}_0^{e(i)} = \mathbb{A} : \overline{\mathbf{B}}^{e(i)}, \quad \text{and} \quad \overline{\mathbf{Z}}_0^{e(i)} = \mathbb{A} : \overline{\mathbf{Z}}^{e(i)}, \tag{C.7}$$

where $\mathbb{A} = \mathbb{I} - \frac{1}{3}\mathbf{I} \otimes \mathbf{I}$ is the fourth order tensor that we used here as an operator to form the deviatoric part of arbitrary second-order tensors. Further, $\overline{\mathbf{B}}^{e(i)}$ is the isochoric part of the elastic left Cauchy-Green tensor defined as $\overline{\mathbf{B}}^{e(i)} = \mathrm{J}^{e(i)-2/3}\mathbf{B}^{e(i)}$, and terms $\overline{g}_0^{e(i)}$ and $\overline{\mathbf{Z}}^{e(i)}$ are defined as

$$\overline{g}_0^{e(i)} = 1 + 4\frac{\mu_a^{EQ}}{\mu_0^{EQ}} \left(\mathrm{tr}\overline{\mathbf{K}}^{e(i)} - 3 \right), \tag{C.8}$$

$$\overline{\mathbf{Z}}^{e(i)} = (\mathbf{n} \otimes \mathbf{n})\, \overline{\mathbf{F}}^{e(i)} \left(\mathbf{I} - \mathbf{n}_0 \otimes \mathbf{n}_0 \right) \overline{\mathbf{F}}^{e(i)T}.$$

For the numerical implementation of Eq.(C.6), we need to introduce the following transformation $\mathbf{F}^{e(i)} = \mathbf{F}\mathbf{F}^{v(i)-1}$ into Eq.(C.7) and Eq.(C.8). Then, we can determine the elastic second Mandel stress tensor Eq.(44) by using Eq.(C.6), which yields

$$\mathbf{M}^{e(i)} = \mu_{(i)}^{NEQ} \mathbf{F}^{e(i)T} \left[\overline{g}_0^{e(i)} \overline{\mathbf{K}}_0^{e(i)} - \left(\frac{m}{a_0} \right) \|\overline{\mathbf{n}}_{\overline{\mathbf{F}}^{e(i)}}\|^2 \overline{a}_{t(i)}^2 \overline{\mathbf{B}}_0^{e(i)} + \overline{a}_{(i)} \overline{\mathbf{Z}}_0^{e(i)} \right] \mathbf{F}^{e(i)-T}. \tag{C.9}$$

The non-equilibrium first Piola-Kirchhoff stress tensor is given as

$$\boxed{\mathbf{P}^{NEQ} = \sum_{i=1}^{M} \mathbf{P}^{e(i)NEQ}.} \tag{C.10}$$

Equilibrium stress tensors

For the equilibrium branch, the first Piola-Kirchhoff stress tensor can be determined by setting $i = 0$ in Eq.(48) or Eq.(C.4),

$$\mathbf{P}^{EQ} = \mu_0^{EQ}\left[\overline{g}_0\overline{\mathbf{K}}_0 - \left(\frac{m}{a_0}\right)\|\overline{\mathbf{n}}_{\overline{\mathbf{F}}}\|^2\overline{a}_t^2\overline{\mathbf{B}}_0 + \overline{a}\overline{\mathbf{Z}}_0\right]\mathbf{F}^{-T} - p\mathrm{J}\mathbf{F}^{-T}, \tag{C.11}$$

in which the hydrostatic pressure $p = -K(\mathrm{J}-1)$ and the deviatoric tensor of the isochoric part of the left Cauchy-Green tensor $\overline{\mathbf{B}}_0$ is given as

$$\overline{\mathbf{B}}_0 = \mathbb{A} : \overline{\mathbf{B}}. \tag{C.12}$$

In addition to the isochoric part of the left Cauchy-Green tensor, the model incorporates two additional deviatoric tensors to account for

$$\overline{\mathbf{K}}_0 = \mathbb{A} : \overline{\mathbf{K}} \quad \text{and} \quad \overline{\mathbf{Z}}_0 = \mathbb{A} : \overline{\mathbf{Z}}, \tag{C.13}$$

in which $\overline{\mathbf{K}}$ is defined in Eq.(61), where

$$\overline{\mathbf{Z}} = (\mathbf{n}\otimes\mathbf{n})\,\overline{\mathbf{F}}\,(\mathbf{I} - \mathbf{n}_0\otimes\mathbf{n}_0)\,\overline{\mathbf{F}}^T. \tag{C.14}$$

Anisotropic contribution to the stress tensor

The anisotropic contribution to the total first Piola-Kirchhoff stress tensor is given as

$$\mathbf{P}^{anis} = 2k_1\left(\overline{I}_4 - 1\right)\exp\left[k_2\left(\overline{I}_4 - 1\right)^2\right]\overline{\mathbf{N}}_0\mathbf{F}^{-T}, \tag{C.15}$$

in which we can define deviatoric part of the tensor $\overline{\mathbf{N}} = \overline{\mathbf{F}}\mathbf{n}_0\otimes\overline{\mathbf{F}}\mathbf{n}_0$ as

$$\overline{\mathbf{N}}_0 = \mathbb{A} : \overline{\mathbf{N}}.$$

Frank and Maxwell's stress tensors

The Frank stress tensor as a part of the first Piola-Kirchhoff stress tensor is determined as

$$\mathbf{P}^{Frank} = \frac{\mathrm{J}K_F}{2}\left[\left(\mathbf{H}\mathbf{F}^{-1} : \mathbf{H}\mathbf{F}^{-1}\right)\mathbf{I} - 2\mathbf{F}^{-T}\mathbf{H}^T\mathbf{H}\mathbf{F}^{-1}\right]\mathbf{F}^{-T}, \tag{C.16}$$

and the Maxwell's stress tensor as

$$\mathbf{P}^{MW} = \mathrm{J}^{-1}\left[\mathbb{D}_n^{-1}\mathbf{F}\mathbf{d}_R\otimes\mathbf{F}\mathbf{d}_R - \frac{1}{2}\left(\mathbb{D}_n^{-1} : \mathbf{F}\mathbf{d}_R\otimes\mathbf{F}\mathbf{d}_R\right)\mathbf{I}\right]\mathbf{F}^{-T}. \tag{C.17}$$

The total first Piola-Kirchhoff stress tensor is determined by summing the contributions given in Eq.(C.6), Eq.(C.11), Eq.(C.16), and Eq.(C.17), yielding the expression from Eq.(C.3) in the form

$$\mathbf{P} = \mathbf{P}^{EQ} + \mathbf{P}^{anis} + \mathbf{P}^{NEQ} + \mathbf{P}^{Frank} + \mathbf{P}^{MW}. \tag{C.18}$$

Appendix C.2. Other constitutive relations

From Eq.(50), we can determine the additional constitutive relations, orientational stress tensor,

$$\mathbf{\Sigma} = \mathrm{J}K_F\mathbf{H}\mathbf{F}^{-1}\mathbf{F}^{-T}, \tag{C.19}$$

the internal director body force

$$\boldsymbol{\pi} = -\left(\mathbf{m}^{EQ} + \mathbf{m}^{NEQ} + \mathbf{m}^{Frank} + \mathbf{m}^{Elec}\right), \tag{C.20}$$

and the following accompanying vectors

$$\mathbf{m}^{EQ} = k\mu_0^{EQ}\overline{g}_0\overline{\mathbf{F}}\mathbf{l}_0\overline{\mathbf{F}}^T\mathbf{n} + \mu_0^{EQ}\overline{a}\overline{\mathbf{F}}(\mathbf{I} - \mathbf{n}_0\otimes\mathbf{n}_0)\overline{\mathbf{F}}^T\mathbf{n}, \tag{C.21}$$

$$\mathbf{m}^{NEQ} = \sum_{i=1}^{M} k\mu_{(i)}^{NEQ}\overline{g}_0^{e(i)}\overline{\mathbf{F}}^{e(i)}\mathbf{l}_0\overline{\mathbf{F}}^{e(i)T}\mathbf{n} + \mu_{(i)}^{NEQ}\overline{a}_{(i)}\overline{\mathbf{F}}^{e(i)}(\mathbf{I} - \mathbf{n}_0\otimes\mathbf{n}_0)\overline{\mathbf{F}}^{e(i)T}\mathbf{n},$$

$$\mathbf{m}^{Frank} = \mathrm{J}K_F\left(\mathbf{F}^{-1}\mathbf{F}^{-T} : \nabla\theta\otimes\nabla\theta\right)\mathbf{n},$$

$$\mathbf{m}^{Elec} = \tilde{\varepsilon}\mathrm{J}^{-1}\left(\mathbf{F}\mathbf{d}_R\otimes\mathbf{F}\mathbf{d}_R\right)\mathbf{n},$$

as well as electric field vector in the form

$$\mathbf{e}_R = \mathrm{J}^{-1}\mathbf{F}^T\mathbb{D}_n^{-1}\mathbf{F}\mathbf{d}_R. \tag{C.22}$$

Appendix D. Reduced form of the balance law for orientational momentum

To reduce computational cost while preserving the accuracy of the presented electro-mechanical model of nematic LCEs, we introduce a reformulation of the second balance law defined in Eq.(A.9). This reformulation relies on the assumption that the director field changes direction only within its initial plane, or equivalently, remains confined to a fixed plane throughout the deformation process. Under this assumption, the director field, its material gradient, and its first time derivative can be represented in the following form:

$$\mathbf{n} = (\cos\theta, \sin\theta, 0)^T, \quad \mathbf{H} = \nabla\mathbf{n} = \mathbf{U}\mathbf{n} \otimes \nabla\theta \quad \text{and} \quad \dot{\mathbf{n}} = \mathbf{U}\mathbf{n}\dot{\theta} \tag{D.1}$$

where θ denotes the orientational angle of the director field, as illustrated in Fig.1a. The associated skew-symmetric tensor is defined as the dual of the unit vector $\mathbf{e}_3$, following the convention introduced in [76],

$$\mathbf{U} = \begin{pmatrix} 0 & -1 & 0 \\ 1 & 0 & 0 \\ 0 & 0 & 0 \end{pmatrix}. \tag{D.2}$$

By taking the scalar product of the directional balance law Eq.(A.9) with the vector $\mathbf{U}\mathbf{n}$, we obtain the reduced form given below:

$$\mathrm{Div}\left(\mathbf{U}\mathbf{n} \otimes \mathrm{J}K_F\mathbf{F}^{-1}\mathbf{F}^{-T}\nabla\theta\right) \cdot \mathbf{U}\mathbf{n} + \boldsymbol{\pi} \cdot \mathbf{U}\mathbf{n} = 0, \tag{D.3}$$

Considering the formula from tensor calculus, $\mathrm{Div}(\mathbf{a} \otimes \mathbf{b}) = (\mathrm{Grad}\mathbf{a})\mathbf{b} + \mathbf{a}\mathrm{Div}\mathbf{b}$ and property $\mathbf{U} : \mathbf{n} \otimes \mathbf{n} = 0$, the final form of the orientational balance law can be obtained after lengthy algebraic manipulations,

$$\mathrm{Div}\boldsymbol{\sigma}^{Frank} + h = 0, \tag{D.4}$$

where

$$\boldsymbol{\sigma}^{Frank} = \mathrm{J}K_F\mathbf{F}^{-1}\mathbf{F}^{-T}\nabla\theta, \tag{D.5}$$

$$h = \boldsymbol{\pi} \cdot \mathbf{U}\mathbf{n} = \mathbf{U} : (\boldsymbol{\pi} \otimes \mathbf{n}) = -\left(\mathbf{m}^{EQ} + \mathbf{m}^{NEQ} + \mathbf{m}^{Frank} + \mathbf{m}^{Elec}\right) \cdot \mathbf{U}\mathbf{n}.$$

Here, $\boldsymbol{\sigma}^{Frank}$ is the reduced orientational stress tensor and h reduced internal director body force. The directional balance law, given in Eq.(D.4), is valid for the nematic LCE model under the assumption that all LC mesogens rotate within a single plane. The reduced natural boundary condition can be obtained by considering Eq.(24) and multiplying it with the vector $\mathbf{U}\mathbf{n}$ as,

$$\boldsymbol{\xi}_R \cdot \mathbf{U}\mathbf{n} = m_\theta, \tag{D.6}$$

where m_θ is an externally applied microscopic torque.

Appendix E. Weak formulation

Finally, we derive the weak form governing equations starting from the balance laws Eq.(72) and Eq.(73), Gauss's law Eq.(74), additional constraints, by multiplying each of them with appropriate test functions:

$$\int_{\mathcal{P}} \left[-\mathbf{P}_{\mathrm{T}} : \mathrm{Grad}\mathbf{w}_1 + (\mathbf{b}_R - \rho_R\mathbf{a}) \cdot \mathbf{w}_1\right] dv_R = 0, \tag{E.1}$$

$$\int_{\mathcal{P}} \left(-\boldsymbol{\sigma}^{Frank} \cdot \mathrm{Grad}w_2 + h \cdot w_2\right) dv_R = 0, \tag{E.2}$$

$$\int_{\mathcal{P}} \left(\mathbf{d}_R \cdot \mathrm{Grad}w_3\right) dv_R = 0, \tag{E.3}$$

while the penalty constraint is given as

$$\int_{\mathcal{P}} \left[\frac{p}{K} + (\mathrm{J} - 1)\right] w_4 dv_R = 0. \tag{E.4}$$

For the time integration of the evolution equation given in Eq.(75), we first formulate its weak form by multiplying it with a test function as follows:

$$\int_{\mathcal{P}} \left\{ \dot{\mathbf{F}}^{v(i)} - \frac{1}{\tau_r^{(i)}} \mathbf{F}^{v(i)-T} \mathbf{F}^T \left[\overline{g}_0^{e(i)} \overline{\mathbf{K}}_0^{e(i)} - \left(\frac{m}{a_0} \right) \| \overline{\mathbf{n}}_{\overline{\mathbf{F}}^{e(i)}} \|^2 \overline{a}_{t(i)}^2 \overline{\mathbf{B}}_0^{e(i)} + \overline{a}_{(i)} \overline{\mathbf{Z}}_0^{e(i)} \right] \mathbf{F}^{-T} \mathbf{C}^{v(i)} \right\} : \mathbf{w}_5 dv_R = 0. \tag{E.5}$$

Here, $\mathbf{w}_5$ is defined as a tensor test function associated with the viscous part of the deformation gradient.

The next step is to apply the implicit backward Euler scheme for time discretization at two time points, t^n and $t^{n+1} = t^n + \Delta t$, directly to $\dot{\mathbf{F}}^{v(i)}$ within the weak form Eq.(E.5),

$$\dot{\mathbf{F}}^{v(i)} \approx \frac{\mathbf{F}_{n+1}^{v(i)} - \mathbf{F}_n^{v(i)}}{\Delta t}, \tag{E.6}$$

where $\Delta t = T/N$ denotes the time increment, where T is the total time interval and N is the number of time steps. By substituting Eq.(E.6) into Eq.(E.5), the final discretized form of the evolution equations can be obtained:

$$\int_{\mathcal{P}} \left\{ \frac{\mathbf{F}_{n+1}^{v(i)} - \mathbf{F}_n^{v(i)}}{\Delta t} \right\} : \mathbf{w}_5 dv_R \tag{E.7}$$

$$- \int_{\mathcal{P}} \left\{ \frac{1}{\tau_r^{(i)}} \mathbf{F}^{v(i)-T} \mathbf{F}^T \left[\overline{g}_0^{e(i)} \overline{\mathbf{K}}_0^{e(i)} - \left(\frac{m}{a_0} \right) \| \overline{\mathbf{n}}_{\overline{\mathbf{F}}^{e(i)}} \|^2 \overline{a}_{t(i)}^2 \overline{\mathbf{B}}_0^{e(i)} + \overline{a}_{(i)} \overline{\mathbf{Z}}_0^{e(i)} \right] \mathbf{F}^{-T} \mathbf{C}^{v(i)} \right\}_{n+1} : \mathbf{w}_5 dv_R = 0,$$

The number of evolution equations, corresponding to the number of branches in the generalized Maxwell model (indexed by $i = 1...M$), can be adjusted during the modeling process in order to fit the experimental results.

References

[1] Pierre-Gilles De Gennes and Jacques Prost. *The Physics of Liquid Crystals*. Number 83 in International Series of Monographs on Physics. Oxford University Press, 1993.

[2] Zoey S Davidson, Hamed Shahsavan, Amirreza Aghakhani, Yubing Guo, Lindsey Hines, Yu Xia, Shu Yang, and Metin Sitti. Monolithic shape-programmable dielectric liquid crystal elastomer actuators. *Science advances*, 5(11):eaay0855, 2019.

[3] Jan Lagerwall. Liquid crystal elastomer actuators and sensors: Glimpses of the past, the present and perhaps the future. *Programmable Materials*, 1:e9, 2023.

[4] Baihong Chen, Lingrui Zhu, Huxiao Yang, and Rui Xiao. A thermo-order-mechanical coupled model for main-chain isotropic-genesis polydomain liquid crystal elastomers. *Mechanics of Materials*, page 105531, 2025.

[5] Rogelio Ortigosa-Martínez, Jesús Martínez-Frutos, Carlos Mora-Corral, Pablo Pedregal, and Francisco Periago. Mathematical modeling, analysis and control in soft robotics: a survey. *SeMA Journal*, 81(1):147–164, 2024.

[6] Elaheh Asgari, Alexandre Robichaud, Paul-Vahé Cicek, and Andy Shih. Liquid crystal elastomers in soft micro electromechanical systems: A review of recent developments. *Journal of Materials Chemistry C*, 12:15359–15381, 2024.

[7] Zhi-Chao Jiang, Qing Liu, Yao-Yu Xiao, and Yue Zhao. Liquid crystal elastomers for actuation: A perspective on structure-property-function relation. *Progress in Polymer Science*, page 101829, 2024.

[8] Antonio DeSimone. Electro-mechanical response of nematic elastomers: an introduction. In *Mechanics and Electrodynamics of Magneto-and Electro-elastic Materials*, pages 231–266. Springer, 2011.

[9] Zhigang Suo. Theory of dielectric elastomers. *Acta Mechanica Solida Sinica*, 23(6):549–578, 2010.

[10] Tongqing Lu, Cheng Ma, and Tiejun Wang. Mechanics of dielectric elastomer structures: A review. *Extreme Mechanics Letters*, 38:100752, 2020.

[11] Rollo Pattinson, Nathan Ellmer, Mokarram Hossain, Rogelio Ortigosa, Jesús Martínez-Frutos, Antonio J Gil, and Anil Bastola. Towards fully 3d printed dielectric elastomer actuators—a mini review. *Additive Manufacturing Letters*, page 100304, 2025.

[12] Giampiero Pampolini and Nicolas Triantafyllidis. Continuum electromechanical theory for nematic continua with application to freedericksz instability. *Journal of Elasticity*, 132:219–242, 2018.

[13] Yiwei Xu and Yongzhong Huo. Continuum modeling of the nonlinear electro-opto-mechanical coupling and solid fréedericksz transition in dielectric liquid crystal elastomers. *International Journal of Solids and Structures*, 219:198–212, 2021.

[14] K Danas, D Mukherjee, K Haldar, and N Triantafyllidis. Bifurcation analysis of twisted liquid crystal bilayers. *Journal of the Mechanics and Physics of Solids*, 123:61–79, 2019.

[15] Yiwei Xu, Yuqian Shen, Yongzhong Huo, and Fan Xu. Spontaneous shear strain governed bending of dielectric nematic elastomer sheets with in-plane director orientation gradients. *Journal of Applied Mechanics*, 92(7):071007, 2025.

[16] Wenzhi Qiu, Yiwei Xu, Fan Xu, and Yongzhong Huo. Programmable electric-field-induced bending shapes of dielectric liquid crystal elastomer sheets. *Extreme Mechanics Letters*, 60:101982, 2023.

[17] Yiwei Xu, Yiqing Zhang, and Yongzhong Huo. Electromechanical deformation of dielectric nematic elastomers accompanied by the rotation of mesogens. *International Journal of Mechanical Sciences*, 218:107061, 2022.

[18] Jinze Zha, Kai Li, and Junxiu Liu. Steady self-spinning of a liquid crystal elastomer-based disc under constant illumination. *International Journal of Solids and Structures*, page 113737, 2025.

[19] Qiang Guo, Yue Zheng, and Shengqiang Cai. Modeling and numerical simulation of thermo-electro-mechanical coupling behaviors of liquid crystal elastomers. *International Journal of Plasticity*, 171:103799, 2023.

[20] Daniel Corbett and Mark Warner. Electromechanical elongation of nematic elastomers for actuation. *Sensors and Actuators A: Physical*, 149(1):120–129, 2009.

[21] Daniel Corbett and Mark Warner. Deformation and rotations of free nematic elastomers in response to electric fields. *Soft Matter*, 5(7):1433–1439, 2009.

[22] EM Terentjev, M Warner, RB Meyer, and J Yamamoto. Electromechanical fredericks effects in nematic gels. *Physical Review E*, 60(2):1872, 1999.

[23] Amir Hossein Rahmati, Kosar Mozaffari, Liping Liu, and Pradeep Sharma. A static and dynamic theory for photo-flexoelectric liquid crystal elastomers and the coupling of light, deformation and electricity. *Journal of the Mechanics and Physics of Solids*, 195:105949, 2025.

[24] Mark Warner and Eugene Michael Terentjev. *Liquid crystal elastomers*, volume 120. Oxford university press, 2007.

[25] L Angela Mihai. *Stochastic elasticity: a nondeterministic approach to the nonlinear field theory*, volume 55. Springer Nature, 2022.

[26] Yang Liu, Qianqian Ji, and Alain Goriely. Surface wrinkling of a hyperelastic half-space coated by a liquid crystal elastomer film. *International Journal of Solids and Structures*, 299:112895, 2024.

[27] Zheliang Wang, Ali El Hajj Chehade, Sanjay Govindjee, and Thao D Nguyen. A nonlinear viscoelasticity theory for nematic liquid crystal elastomers. *Journal of the Mechanics and Physics of Solids*, 163:104829, 2022.

[28] L Angela Mihai, Devesh Mistry, Thomas Raistrick, Helen F Gleeson, and Alain Goriely. A mathematical model for the auxetic response of liquid crystal elastomers. *Philosophical Transactions of the Royal Society A*, 380(2234):20210326, 2022.

[29] Virginia Agostiniani and Antonio DeSimone. Ogden-type energies for nematic elastomers. *International Journal of Non-Linear Mechanics*, 47(2):402–412, 2012.

[30] Nurul Hassan Shah and Shaikh Faruque Ali. A constitutive framework for modelling elastomers, soft tissues and liquid crystal elastomers. *Proceedings of the Royal Society A*, 481(2312):20250017, 2025.

[31] Afshin Anssari-Benam and Giuseppe Saccomandi. A model for capturing the rate-dependent mechanical behaviour of liquid crystal elastomers. *Mechanics of Materials*, 198:105108, 2024.

[32] Sergio Conti, Antonio DeSimone, and Georg Dolzmann. Semisoft elasticity and director reorientation in stretched sheets of nematic elastomers. *Physical Review E*, 66(6):061710, 2002.

[33] Devesh Mistry, Philip B Morgan, John H Clamp, and Helen F Gleeson. New insights into the nature of semi-soft elasticity and "mechanical-fréedericksz transitions" in liquid crystal elastomers. *Soft Matter*, 14(8):1301–1310, 2018.

[34] GC Verwey and Mark Warner. Compositional fluctuations and semisoftness in nematic elastomers. *Macromolecules*, 30(14):4189–4195, 1997.

[35] Yang Zhang, Zhiyuan Zhang, and Yongzhong Huo. Nucleation and critical conditions for stripe domains in monodomain nematic elastomer sheets under uniaxial loading. *Journal of the Mechanics and Physics of Solids*, 144:104110, 2020.

[36] Yang Zhang, Chen Xuan, Yuefeng Jiang, and Yongzhong Huo. Continuum mechanical modeling of liquid crystal elastomers as dissipative ordered solids. *Journal of the Mechanics and Physics of Solids*, 126:285–303, 2019.

[37] Yu Zhou, Chen Wei, and Lihua Jin. A modified semi-soft model of liquid crystal elastomers: Application to elastic and viscoelastic responses. *Journal of the Mechanics and Physics of Solids*, 196:106027, 2025.

[38] Cristina P Martin Linares, Nicholas A Traugutt, Mohand O Saed, Alejandro Martin Linares, Christopher M Yakacki, and Thao D Nguyen. The effect of alignment on the rate-dependent behavior of a main-chain liquid crystal elastomer. *Soft Matter*, 16(38):8782–8798, 2020.

[39] Chen Wei, Scott Cao, Yu Zhou, Dehao Lin, and Lihua Jin. Rate-dependent stress-order coupling in main-chain liquid crystal elastomers. *Soft Matter*, 19(41):7923–7936, 2023.

[40] Christopher Chung, Chaoqian Luo, Christopher M Yakacki, Bo Song, Kevin Long, and Kai Yu. Revealing the unusual rate-dependent mechanical behaviors of nematic liquid crystal elastomers. *International Journal of Solids and Structures*, 292:112712, 2024.

[41] Xin Wang, Jiatong Han, Hongtu Xu, Haibo Ji, Zengshen Yue, Rui Zhang, Bingyang Li, Yan Ji, Zhen Li, Pengfei Wang, et al. Nonlinear mechanical behaviour and visco-hyperelastic constitutive description of isotropic-genesis, polydomain liquid crystal elastomers at high strain rates. *Journal of the Mechanics and Physics of Solids*, 193:105882, 2024.

[42] Ali El Hajj Chehade, Beijun Shen, Chris M Yakacki, Thao D Nguyen, and Sanjay Govindjee. Finite element modeling of viscoelastic liquid crystal elastomers. *International Journal for Numerical Methods in Engineering*, 125(16):e7510, 2024.

[43] L Rezaei, G Scalet, M Peigney, and A Azoug. Coupling between viscoelasticity and soft elasticity in main-chain nematic liquid crystal elastomers. *Journal of the Mechanics and Physics of Solids*, 187:105612, 2024.

[44] Victoria Lee, Adeline Wihardja, and Kaushik Bhattacharya. A macroscopic constitutive relation for isotropic-genesis, polydomain liquid crystal elastomers. *Journal of the Mechanics and Physics of Solids*, 179:105369, 2023.

[45] Morton E Gurtin, Eliot Fried, and Lallit Anand. *The mechanics and thermodynamics of continua*. Cambridge university press, 2010.

[46] Gerhard A Holzapfel. Nonlinear solid mechanics: a continuum approach for engineering science, 2002.

[47] PJ128117 Flory. Thermodynamic relations for high elastic materials. *Transactions of the Faraday Society*, 57:829–838, 1961.

[48] Frank M Leslie. Continuum theory for nematic liquid crystals. *Continuum Mechanics and Thermodynamics*, 4(3):167–175, 1992.

[49] David R Anderson, Donald E Carlson, and Eliot Fried. A continuum-mechanical theory for nematic elastomers. *Journal of Elasticity*, 56:33–58, 1999.

[50] Iain W Stewart. *The static and dynamic continuum theory of liquid crystals: a mathematical introduction*. Crc Press, 2019.

[51] Victor A Eremeyev, Leonid P Lebedev, and Holm Altenbach. *Foundations of micropolar mechanics*. Springer Science & Business Media, 2012.

[52] Vlado A Lubarda. Constitutive theories based on the multiplicative decomposition of deformation gradient: Thermoelasticity, elastoplasticity, and biomechanics. *Appl. Mech. Rev.*, 57(2):95–108, 2004.

[53] Jacob Lubliner. A model of rubber viscoelasticity. *Mechanics Research Communications*, 12(2):93–99, 1985.

[54] Stefanie Reese and Sanjay Govindjee. A theory of finite viscoelasticity and numerical aspects. *International journal of solids and structures*, 35(26-27):3455–3482, 1998.

[55] Eric M Stewart and Lallit Anand. A large deformation viscoelasticity theory for elastomeric materials and its numerical implementation in the open-source finite element program fenicsx. *International Journal of Solids and Structures*, 303:113023, 2024.

[56] Zeng Liu, Rogelio Ortigosa, Antonio J Gil, and Javier Bonet. Large strain constitutive modelling of soft compressible and incompressible solids: Generalised isotropic and anisotropic viscoelasticity. *Journal of the Mechanics and Physics of Solids*, page 106194, 2025.

[57] Yunwei Mao, Shaoting Lin, Xuanhe Zhao, and Lallit Anand. A large deformation viscoelastic model for double-network hydrogels. *Journal of the Mechanics and Physics of Solids*, 100:103–130, 2017.

[58] Lallit Anand. A cahn–hilliard-type theory for species diffusion coupled with large elastic–plastic deformations. *Journal of the Mechanics and Physics of Solids*, 60(12):1983–2002, 2012.

[59] Robert M McMeeking and Chad M Landis. Electrostatic forces and stored energy for deformable dielectric materials. *Journal of Applied Mechanics*, 72(7):581–590, 2005.

[60] Robert M McMeeking, Chad M Landis, and Salomon MA Jimenez. A principle of virtual work for combined electrostatic and mechanical loading of materials. *International Journal of Non-Linear Mechanics*, 42(6):831–838, 2007.

[61] A Cemal Eringen. *Microcontinuum field theories: I. Foundations and solids*. Springer Science & Business Media, 2012.

[62] Rastko Stojanović. *Recent Developments in the Theory of Polar Continua: Course held at the Department for Mechanics of Deformable Bodies, June–July 1970*, volume 27 of *CISM International Centre for Mechanical Sciences, Courses and Lectures*. Springer-Verlag, Vienna, Vienna, Austria, 1st edition, 1970.

[63] Rastko Stojanović. Nonlinear micropolar elasticity. In W. Nowacki and W. Olszak, editors, *Micropolar Elasticity*, volume 151 of *CISM Courses and Lectures*, pages 73–103. Springer, Vienna, 1974.

[64] Samuel C Lamont and Franck J Vernerey. Generalized continuum theory for nematic elastomers: Non-affine motion and characteristic behavior. *Journal of the Mechanics and Physics of Solids*, 190:105718, 2024.

[65] Hüsnü Dal, Alp Kağan Açan, Ciara Durcan, and Mokarram Hossain. An in silico-based investigation on anisotropic hyperelastic constitutive models for soft biological tissues. *Archives of Computational Methods in Engineering*, 30(8):4601, 2023.

[66] Alexander Ricker, Meike Gierig, and Peter Wriggers. Multiplicative, non-newtonian viscoelasticity models for rubber materials and brain tissues: numerical treatment and comparative studies. *Archives of computational methods in engineering*, 30(5):2889–2927, 2023.

[67] Martin Alnæs, Jan Blechta, Johan Hake, August Johansson, Benjamin Kehlet, Anders Logg, Chris Richardson, Johannes Ring, Marie E Rognes, and Garth N Wells. The fenics project version 1.5. *Archive of numerical software*, 3(100), 2015.

[68] Eric M. Stewart, Shawn A. Chester, and Lallit Anand. Example codes for coupled theories in solid mechanics. https://doi.org/10.5281/zenodo.14680877, January 2025. Version v0.

[69] Shuolun Wang, Martina Decker, David L Henann, and Shawn A Chester. Modeling of dielectric viscoelastomers with application to electromechanical instabilities. *Journal of the Mechanics and Physics of Solids*, 95:213–229, 2016.

[70] Weida Kang, Qian Cheng, Changyue Liu, Zhijian Wang, Dongfeng Li, and Xudong Liang. A constitutive model of monodomain liquid crystal elastomers with the thermal-mechanical-nematic order coupling. *Journal of the Mechanics and Physics of Solids*, 196:105995, 2025.

[71] Jinxiong Zhou, Wei Hong, Xuanhe Zhao, Zhiqian Zhang, and Zhigang Suo. Propagation of instability in dielectric elastomers. *International Journal of Solids and Structures*, 45(13):3739–3750, 2008.

[72] Luis Dorfmann and Ray W Ogden. Instabilities of soft dielectrics. *Philosophical Transactions of the Royal Society A*, 377(2144):20180077, 2019.

[73] Chennakesava Kadapa and Mokarram Hossain. A robust and computationally efficient finite element framework for coupled electromechanics. *Computer Methods in Applied Mechanics and Engineering*, 372:113443, 2020.

[74] Liping Liu. An energy formulation of continuum magneto-electro-elasticity with applications. *Journal of the Mechanics and Physics of Solids*, 63:451–480, 2014.

[75] Shengyou Yang, Xuanhe Zhao, and Pradeep Sharma. Revisiting the instability and bifurcation behavior of soft dielectrics. *Journal of Applied Mechanics*, 84(3):031008, 2017.

[76] Roman Poya, Antonio J Gil, Rogelio Ortigosa, and Roberto Palma. On a family of numerical models for couple stress based flexoelectricity for continua and beams. *Journal of the Mechanics and Physics of Solids*, 125:613–652, 2019.